COMPUTATIONAL AND EXPERIMENTAL STUDY ON LiTaO3 NANOPARTICLES FOR NEAR-INFRARED DETECTORS AND BORON NITRIDE NANOPARTICLES FOR GAS SENSING

A Dissertation

by

ANDREA PELAYO CARVAJAL

Submitted in Partial Fulfillment of the

Requirements for the Degree of

DOCTOR OF PHILOSOPHY

Major Subject: Physics

University of Texas Rio Grande Valley
July 2026

COMPUTATIONAL AND EXPERIMENTAL STUDY ON LiTaO3 NANOPARTICLES FOR NEAR-INFRARED DETECTORS AND BORON NITRIDE NANOPARTICLES FOR GAS SENSING

A Dissertation
by
ANDREA PELAYO CARVAJAL

COMMITTEE MEMBERS

Dr. Nicholas Dimakis
Chair of Committee

Dr. Constantine Tarawneh
Co-Chair of Committee

Dr. Mkhitar Hobosyan
Committee Member

Dr. Sanju Gupta
Committee Member

July 2026

ABSTRACT

Pelayo Carvajal, Andrea. Computational and Experimental Study on LiTaO3 Nanoparticles For Near-Infrared Detectors And Boron Nitride Nanoparticles for Gas Sensing. Doctor of Philosophy (PhD), July 2026, 90 pp.,1 table, 36 figures, 174 references.

The development of reliable sensing materials is essential for infrastructure maintenance and early-warning detection technologies. This work investigates two ceramic-based sensing materials: rare-earth-doped lithium tantalate ($LiTaO_3$, LT) for near-infrared optical sensing relevant to crack detection, and silver-modified hexagonal boron nitride nanocomposites (Ag/defect h-BN) for carbon monoxide (CO) gas sensing. A computational and experimental approach was used to evaluate their structural, electronic, optical, and sensing properties.

Density functional theory (DFT) was used to study various rare-earth doped LT configurations, while GW-Bethe–Salpeter equation (GW-BSE) calculations were used to investigate the electronic and optical properties of pristine, defective, and Ag-modified defect h-BN. In LT, rare-earth doping introduced localized 4f states that modified the electronic structure and tunable optical response. Quantum Theory of Atoms in Molecules (QTAIM) and Electron Localization Function (ELF) analyses were used to characterize chemical bonding and electron localization in the doped LT structures. For Ag/defect h-BN, band-structure and optical property calculations showed that CO adsorption is strongly defect-dependent. CO binds strongly at Ag-decorated B-vacancy sites, whereas the interaction is weak at Ag-decorated N-vacancy sites.

Experimentally, LT-based powders and Ag/h-BN nanocomposites were synthesized and characterized by X-ray diffraction (XRD), Scanning Electron Microscopy (SEM), Photoluminescence (PL), and conductivity measurements. The Ag/h-BN nanocomposites exhibited preliminary CO-responsive conductive behavior. The h-BN-30 wt.% Ag pellet showed a decrease in conductivity during CO exposure, followed by a recovery during purging. In contrast, the h-BN-80 wt.% Ag pellet showed an incomplete recovery under the present test conditions, indicating that a higher Ag content hinders reversibility.

Overall, rare-earth doping was shown to tune the optical response of LT for near-infrared crack detection, while Ag incorporation enhanced the CO-sensing performance of defect h-BN-based ceramic nanocomposites. These findings demonstrate the potential of advanced ceramic nanomaterials for optical and gas-sensing applications in structural health and environmental monitoring.

DEDICATION

This dissertation is dedicated to my parents for their unconditional love and never-ending support. Dad, everything I have accomplished is thanks to your devotion to our family and your unwavering ability to work hard despite adversity. Mami, esto te lo dedico con todo el amor del mundo; sin tus sacrificios, yo no habría podido llegar hasta aquí. This is also dedicated to my sisters, Rebeca and Jessica. Rebeca, without your infectious dedication and lifelong support for my dreams, I would not be here today. Jessica, this achievement was only possible because of your charisma and the sense of purpose you bring to my life. Lastly, this is dedicated to Nanook, for his emotional support and constant reminders to sleep.

ACKNOWLEDGEMENTS

I would like to express my sincere gratitude and appreciation to my advisor, Dr. Nicholas Dimakis, for his unwavering support and guidance throughout my education and research. I am also deeply grateful to Dr. Mkhitar Hobosyan and Dr. Constantine Tarawneh for the invaluable opportunities they have provided me since my undergraduate studies. Finally, I want to formally thank my external committee member, Dr. Sanju Gupta, for participating in my dissertation defense and providing such valuable feedback.

Honorable mention goes to all faculty, staff, and peers who have assisted and accompanied me in this academic journey.

I would like to acknowledge funding provided by the National Science Foundation CREST Center for Multidisciplinary Research Excellence in Cyber-Physical Infrastructure Systems (NSF Award No. 2112650).

I would also like to acknowledge the Texas Advanced Computing Center (TACC) at The University of Texas at Austin for providing HPC resources that have contributed to the research results reported within this paper. URL: http://www.tacc.utexas.edu.

TABLE OF CONTENTS

Page

LIST OF FIGURES

Page

CHAPTER I

INTRODUCTION

Infrastructure degradation results from local material failures and environmental factors. This problem is particularly prevalent in urban areas, where a growing population demands more accessible housing, utilities, and transportation. Consequently, as new infrastructure is built, older structures are often neglected, leaving them frail and vulnerable to disasters. The risk of deterioration cannot be eliminated, yet a good maintenance program will extend the lifespan of infrastructure [1, 2]. Routine inspections are key to early-crack detection in all man-made structures [3, 4]. Federal regulations mandate visual crack characterization assessments every two years, with more frequent inspections required if widespread deterioration is detected [5, 6]. Each visual bridge inspection includes an assessment of the structural type of the bridge, construction materials, condition rating, load rating, roadway data, and clearances [7-9]. With every assessment, engineers are required to evaluate the state of urgency on a 0–9 scale [10]. Aside from inconsistencies and a tendency to make errors in analysis [8], the qualifications and responsibilities of an inspector are taxing and entail limitations on access to critical regions of the infrastructure being assessed [11]. This could lead to an inaccurate evaluation and, more critically, compromise the safety of the inspector. Automation addresses these challenges and enables efficient, accurate, and periodic inspections.

Developing quasi-real-time crack detection techniques capable of accurately assessing the type, depth, and location of degradation is of great importance. In the late 1990s, Rens *et al*. emphasized the importance of reviewing contemporary Nondestructive Evaluation (NDE) inspection techniques and evaluating their effectiveness for civil engineering structures [12]. Some of the best-suited methods included acoustic emission, thermal, ultrasonic, and magnetic [13].

Acoustic emission (AE) monitors transient elastic waves produced by the rapid release of energy during a crack and radiated through the structure [12]. AE is highly sensitive to active defects and can localize such through a series of mounted sensors, but it does not directly provide detailed crack geometry or depth profiling, which is critical for complex crack profiles. Furthermore, AE sensors require careful signal processing and source discrimination to separate relevant emissions from background noise [14, 15]. Ultrasonic methods work similarly by flooding the structure with ultrasound pulses and can potentially provide crack profiling, but require skilled interpretation [16]. Magnetic techniques are only effective for detecting surface cracks in ferromagnetic or conductive materials [17]. Moreover, other challenges lie with the repair and replacement of a malfunctioning sensor. Thermal (infrared) thermography is a noncontact technique that does not require adhesion to the structure.

Among the various NDE techniques, infrared thermography monitors surface temperature variations related to deterioration, offering rapid, wide-area screening [18]; building on these capabilities, advancements in sensor technology have introduced near-infrared (NIR) laser sensing as a viable and complementary alternative for high-resolution surface mapping and detection of surface texture [19]. NIR spectra cover wavelengths from 800–2500 nm, beyond the visible spectrum. NIR-laser-based sources offer higher accuracy through optical methods such as

laser triangulation, as it reduces interference from ambient light, enabling higher-resolution surface mapping and more reliable texture detection [20, 21].

With a growing population and rising demand for accessible housing, utilities, and transportation, vehicle use naturally increases. Consequently, living organisms are constantly exposed to an atmospheric mixture that includes both essential and harmful components, such as carbon monoxide (CO). CO intoxication remains one of the most studied because CO competes with oxygen for binding to hemoglobin, earning the name “silent killer” [22, 23]. Consequently, the development of highly sensitive, selective, and reusable gas sensors capable of rapid, reliable CO detection across multiple sensing cycles is essential for environmental monitoring, industrial safety, and public health.

Gas sensors are characterized by multiple performance parameters, including durability, thermal stability, rapid detection, and quick recovery [24]. Traditional ceramics provide the mechanical properties of durability and toughness required for the listed functions, as well as sensor longevity and performance [25]. However, advanced ceramic sensors are used where greater emphasis is placed on meeting electrical, thermal, magnetic, and optical requirements. Advanced ceramics are primarily based on groups of oxides, non-oxides, or their combinations. The principle behind the use of oxides is to detect gases such as CO, methane (CH_4), carbon dioxide (CO_2), and many others [25]. The gas-sensing mechanism of these sensors relies on interactions that occur after the adsorption of atmospheric oxygen. The interaction will cause a chemical change within the material and alter the conductivity [26].

The proposed research focuses on candidate materials for improved crack and gas detection technologies, which could significantly improve the safety, efficiency, and cost-effectiveness of infrastructure maintenance.

CHAPTER II

LITERATURE REVIEW

2.1 Rare-Earth-Doped and Pure Lithium Tantalate for Crack Detection

The basic operating principle of laser triangulation involves an emitter- receiver subsystem, in which a laser beam is directed toward a test surface and, upon interaction, is reflected onto the receiver [24-26]. Any surface flaw disrupts this optical path. Because a primary goal of this work is to utilize NIR laser sensing techniques for high-resolution surface mapping and texture detection, ensuring absolute precision in the positioning and actuation of these optical components is important.

Characterized by electrical polarization in response to mechanical stress, piezoelectric and ferroelectric materials are crucial for enabling nonlinear optical effects that help generate light waves at new frequencies [27, 28]. In 1949, lithium tantalate ($LiTaO_3$; LT) was discovered as a member of a new class of ferroelectric materials adopting the ilmenite crystal structure [29]. Although both perovskites and ilmenites share a general formula of ABO_3, perovskites feature a cubic arrangement, while ilmenites adopt a rhombohedral structure, which is a subset of the trigonal crystal system [30]. This is shown in Figure 1. The lack of a center of symmetry in ilmenites like LT results in a pyroelectric effect, generating electric polarization when subjected to a temperature change.

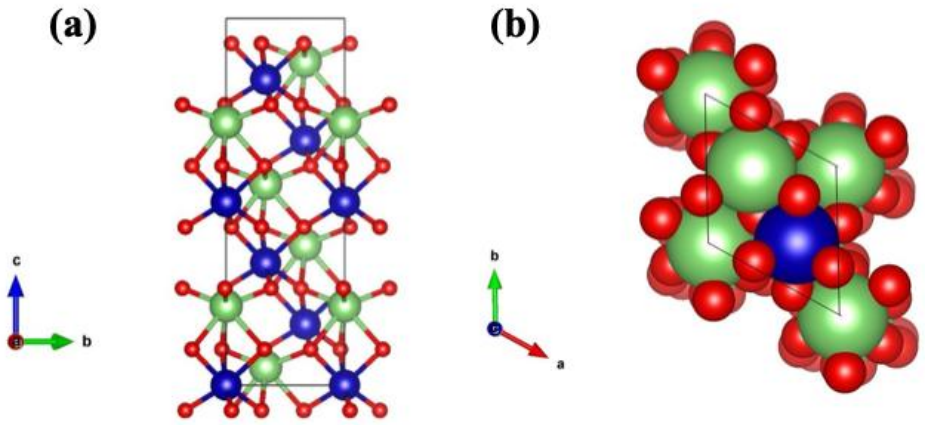

Figure 1. LT unit cell (a) side view and (b) top view. Atoms are colored as follows: Li, green; Ta, blue; O, red. The thin lines denote the unit cell boundaries.

From the unit cell, the high density of oxygen is one of the most important factors regarding the ferroelectricity of LT [31]. Figure 1b shows a tightly packed oxygen atom that allows positively charged lithium and tantalum ions to easily shift from their centrosymmetric positions, which is essential for generating spontaneous electric polarization. The oxygen atoms, being highly electronegative, will stabilize the charge distribution within the material. This is an important aspect in ferroelectricity as LT allows spontaneous polarization to be reversed by an electric field [32]. For sensing applications, LT is a strong candidate among materials used in pyroelectric detectors, as it has a high Curie temperature (the temperature at which it loses its pyroelectric properties) and a high pyroelectric coefficient [33-35].

A variety of synthetic methods have been reported to produce LT. The Double Crucible Czochralski (DCCZ) method presented by Furukawa *et al*. [36] uses appropriate proportions of Tantalum Oxide (Ta_2O_5) and Lithium Carbonate (Li_2CO_3), which are mixed in a ball mill and later calcinated at a high temperature of 1000°C for 12 hours. The powder is simultaneously

pressed and heated to 1250°C to obtain coarse LT grains. This powder is fed into the Czochralski furnace along with Li-rich powder (prepared under the same conditions), and the mixture is heated to obtain a crack-free crystal of 45 mm in diameter. Although the DCCZ method produces high-quality crystals, the process is significantly challenging [37] and is not necessary for sensing applications that require smaller crystal dimensions.

Another synthesis method for stoichiometric LT powder is by a solid-state combustion route. As the name suggests, solid-state combustion synthesis focuses on the formation of solids through highly exothermic (heat-releasing) reactions between mixed compounds [38]. Obtaining pure LT is challenging via conventional solid-state combustion, as it requires a high temperature of 1250°C and a long heat treatment of 48 hours. Zhu *et al*. [39] incorporate urea into the Tantalum Oxide (Ta_2O_5) and Lithium Carbonate (Li_2CO_3) mixture as a fuel to reduce reaction time. The reaction times were measured at 500°C, 600°C, 650°C, 700°C, and 800°C. Compared with a conventional solid-state combustion, the use of urea reduced the calcinating temperature to 700°C in only 6 hours of heat treatment. However, the Scanning Electron Microscope (SEM) analysis revealed particle-size inhomogeneity and a mixture of nano-, micro-, and LT flakes.

For the fabrication of nano-sized particles, a wet-chemical synthesis route is better suited. In 2008, Muthurajan *et al*. [40] reported the production of LT nano-sized powder at a calcinating temperature of 450°C for 6 hours. Although the particle morphology was irregular, the powder had an average particle size of 50 nanometers (nm).

Numerous studies have demonstrated that incorporating various rare-earth dopants into the LT host yields new optoelectronic properties. Rare earth elements, also known as the lanthanides, are characterized by the filling of the 4f subshell. The elements in this group possess orbitals that facilitate unique electronic transitions, enabling the emission and absorption of

specific higher-energy wavelengths [41]. Yang *et al*. [42] synthesized submicron Erbium (Er^{3+})-doped LT particles via solid-state combustion, demonstrating Er^{3+}-doped LT yields optimal near-infrared (NIR) emissions. Shi *et al*. [43] state that Er^{3+}-doped LT combines the lasing properties of Er^{3+} with the nonlinear optical properties of LT. Li *et al*. [44] demonstrated that co-doping LT with Praseodymium (Pr^{3+}) and Gadolinium (Gd^{3+}) led to a significant increase in the mechanoluminescence and photostimulated luminescence of the material.

This study adopts a wet-chemical synthesis approach to fabricate LT nanoparticles and focuses on the characterization of their optical and electronic properties, which extend into the NIR range upon doping and co-doping with Er^{3+} and Pr^{3+} at varying concentrations. A detailed account of the synthesis protocols is provided in the Sample Preparation section.

2.2 Hexagonal Boron Nitride for Gas Detection

As previously mentioned, gas sensors are characterized by several performance parameters, including durability, thermal stability, rapid detection, and quick recovery [24]. Gas sensing can be classified into two main categories: (1) methods based on electrical variation upon contact with the gas and (2) those based on other types of physical or chemical variation [45].

Prominent gas detection methodologies based on physical or chemical changes encompass optical sensing, acoustic analysis, and gas chromatography. Optical gas-sensing techniques are diverse and can be configured to detect a wide range of toxic gases [46]. Absorption-based techniques use a light source passing through a gas toward two filters: one covering the absorption band of the target gas and the other serving as a reference. However, the limitations of optical gas sensing include high cost, limited wavelength coverage, and reduced

effectiveness in multi-gas detection, which stems from a degrading signal-to-noise ratio [47]. Acoustic sensors operate when a piezoelectric substrate is exposed to a gas, prompting metal transducers to launch acoustic waves at specific frequencies. The type of wave generated depends on the crystal orientation and thickness of the piezoelectric material [48]. However, the primary challenge facing acoustic sensors is their inability to maintain long-term stability during field testing due to dependence on temperature and humidity [49]. Gas chromatography separates sample compounds based on their retention in the column [50]. Although highly accurate, it is expensive and is used for laboratory testing rather than field deployment [45].

Electrical variation-based gas-sensing methodologies primarily utilize employ metal oxide/metallic nanostructures, conductive polymers, and carbon nanomaterials [51]. An electrochemical sensor detects gas by measuring the oxidation or reduction current produced when the target gas reacts with the sensing material [52]. Conductive polymers can be tuned for electrical conductivity through material doping or chemical structural modification [53]. This sensing method has shown promise across a wide range of applications, including medicinal diagnostics [54] and food safety monitoring [55]. However, further improvements in conductive polymer gas sensors are still needed to enhance gas detection sensitivity and selectivity [56, 57]. Carbon nanomaterials possess high surface-to-volume ratios alongside unique electrical, optical, and mechanical properties that make them highly desirable for sensing applications [58]. However, fabrication remains a challenge, and research is needed to find cost-effective, scalable production methods without compromising the properties of carbon nanomaterials [59]. Lastly, metal oxide semiconductors are the most prominent gas-sensing materials due to their low-cost and high sensitivity [45]. Major challenges for semiconductor metal oxide gas sensors include

gas selectivity and the trade-off between sensitivity and structural stability, as reducing material size compromises its structural integrity [60].

With their exceptional durability, robustness, and high-temperature tolerance, ceramic gas sensors are well-suited for field testing [61, 62]. Traditional ceramics are formed from using raw materials, most commonly clays [63]. Traditional ceramics exhibit the mechanical properties of durability and toughness required in sensors, thereby providing sensor longevity and performance [25]. Advanced ceramics are modern or modified traditional materials engineered for precise optical and electrical properties while retaining core ceramic characteristics [64]. One of the measured quantities sensitive to the presence of gases is resistance, in which gas interaction can trigger a chemical reaction within the material and alter its electrical conductivity [65]. This transient resistance response shows immediate peak detections proportional to the target gas concentration. The testing protocol cycles the sensor between clean air and a fixed gas concentration, facilitating multi-cycle evaluation [62].

Titanium Oxide (TiO_2), Zinc Oxide (ZnO), and Tin Oxide (SnO_2) are some ceramic materials used for gas sensing [66]. In addition to stoichiometric TiO_2, numerous non-stoichiometric configurations have been identified, many of which exhibit highly promising gas-sensing properties [67]. Pure TiO_2-based gas sensors exhibit high resistance, leading to poor sensing performance. Therefore, TiO_2 is coupled with semiconducting materials to achieve increased sensitivity, lower operating temperature, and faster response time [68, 69]. The main challenge for TiO_2-based gas sensors remains the control of stoichiometry and morphology for pure and doped TiO_2 [67, 70].

ZnO nanostructures with varying morphologies have been extensively studied for gas sensing applications due to their high electron mobility, high surface area, and good chemical

and thermal stability [71]. Various ZnO nanostructures enhance selectivity, shorten recovery time, and provide faster response times [72-75]. However, high operating temperatures remain a challenge even when coupled with silver (Ag) nanoparticles [76].

Among the ceramics discussed, SnO_2 is the most widely used metal oxide in gas-sensing applications. Its excellent electrical and optical properties and good chemical stability make SnO_2 a suitable material [77]. The basic detection principle of SnO_2 is governed by the adsorption of oxygen species and the resulting depletion layer at the surface. Consequently, it will alter the conductivity of SnO_2 in proportion to the gas concentration [78]. The operating temperature of SnO_2-based sensors ranges from 25°C to 500°C, depending on the target gas [79]. As with TiO_2, the challenge remains the control of stoichiometry and morphology in SnO_2-based sensors.

Among these materials, hexagonal boron nitride (*h*-BN) is a promising candidate for gas-sensing applications due to its high specific surface area, exceptional thermal stability, and chemical inertness [80-82]. Although *h*-BN is an insulating ceramic, incorporating a metal can enhance the catalytic performance of the material, thereby altering the band structure and improving sensor responsiveness [83-87]. Lin *et al*. [88] performed density functional theory (DFT) calculations to evaluate how introducing metal atoms into *h*-BN vacancies enhances the catalytic performance of the material. For CO, Ag exhibited a lower binding energy of -1.07 eV compared to the other investigated metals, indicating weaker adsorption. For gas-sensing applications, weak adsorption is highly advantageous, as it facilitates gas leaving the system, thereby promoting faster sensor recovery times and preventing saturation. Furthermore, nanostructured *h*-BN would enhance the sensitivity. Feng *et al*. [89] and Lin *et al.*[90]

experimentally demonstrated that *h*-BN nanostructures show repeatability, fast response and recovery times, and can operate in harsh conditions.

In this study, we utilize DFT to investigate the electronic structure, dielectric functions, and optical properties of pure *h*-BN, defective *h*-BN, and Ag/*h*-BN nanocomposite. Furthermore, we experimentally synthesize and evaluate the electrochemical response of the nanocomposite upon exposure to CO, thereby assessing its viability as a gas-sensing ceramic material.

CHAPTER III

COMPUTATIONAL AND EXPERIMENTAL METHODS

3.1 Theoretical Framework

3.1.1 Overview on Density Functional Theory

A fundamental understanding of a material is achieved by analyzing the quantum behavior of its constituent atoms and molecules, including their energy states and interactions. In classical mechanics, specifying the position of an object determines its velocity, momentum, and energy, reflecting the reversible nature of classical processes. Yet, nature is more than that. Prigogine suggests irreversibility as an illusion caused by a lack of knowledge of the dynamical nature of the system [91]. Quantum mechanics describes physical systems through a wave function obtained by the Schrödinger equation [92]. This wave function admits a time-reversible dynamical interpretation, resembling a classical view [93]. A complete description of the Schrödinger equation is [94]

$$\left[-\left(\frac{\hbar^2}{2m}\right) \Sigma \nabla_i^2 \; + \; \Sigma \, V(r_i) \; + \; \Sigma U(r, r\} \right] \psi(r) = \; E \, \psi(r), \tag{1}$$

The three terms within the brackets of this equation correspond to the following physical meaning. The first term represents the kinetic energy operator, describing the motion of individual electrons. The second term accounts for the interaction between each electron and the collection of atomic nuclei, typically modeled as an external electrostatic potential that confines

the electronic states. The third term describes the interactions between electrons, the Coulomb repulsion, which couples their motion and gives rise to many-body effects [92, 95, 96]. Schrödinger's matter waves represent an N-particle system in a 3N-dimensional space, providing a complete visualization of all couplings; solving the resulting equations has been prohibitively difficult in many-electron systems [96]. It is possible to address the issue using a self-consistent field (SCF) approach. The assumption made by Hartree is that the wave function for the second electron within a two-electron system is independent of the coordinates of the first electron [97-99].

$$\psi = \psi_1(r)\psi_2(r), \dots, \psi_N(r) \tag{2}$$

Moreover, the Hartree product neglects exchange, relativity, and spin effects. This is highly important for future discussion. This theory is refined by the concept of exchange energy, which incorporates the antisymmetry of electrons proposed by Fock [100, 101]. The omission of antisymmetry allows for an unphysical wavefunction that does not change when particles are swapped [102]. While Hartree and Fock's efforts on employing a tractable approximation to the many-wave function do not go unrecognized, the wavefunction itself does not carry a direct physical interpretation, yet, when squared, it gives rise to the joint probability distribution for all N electrons [94].

$$probability\ density = |\psi(r_1, r_2, \dots, r_N)|^2 = \psi(r_1, r_2, \dots, r_N)\psi^*(r_1, r_2, \dots, r_N), \tag{3}$$

A closely related quantity is the density of electrons at a position in space and is given by [94]

$$\rho(r) = 2\sum \psi(r_1, r_2, \dots, r_N)\psi^*(r_1, r_2, \dots, r_N) \tag{4}$$

where the factor of two accounts for the Pauli exclusion principle in spin degeneracy. According to Hohenberg-Kohn-Sham, all information about the system can be obtained by a knowledge of the ground-state density. Into this principle, a universal functional is applied to all electronic systems in the ground state, despite the external potential [103, 104].

$$E[\rho] = T_s[\rho] + \int v(r)\rho(r)dr + E_{ee}^{KS}[\rho], \tag{5}$$

where the quantities of the ground-state energy are as follows, the electron-charge density is defined as ρ, the kinetic energies $T_s[\rho]$, and the energy functional for a given potential $v(r)$. The electron-energy functional incorporates the effects of Pauli exchange, Coulomb repulsion, and additional correlation contributions beyond the non-interacting kinetic energy [104-106]. By reformulating the interacting many-electron problem in terms of the electron density and introducing a non-interacting reference system, the Kohn–Sham formalism provides a practical and computationally tractable route to determining ground-state properties while retaining the essential physics of electron interactions. The ground-state energy is redefined as [106]

$$E[\rho] = \int v(r)\rho(r)dr + \frac{1}{2}\int \frac{\rho(r)\rho(r')}{|r-r'|}drdr' + G[\rho] \tag{6}$$

The first part of the second integral, the classical piece, corresponds to Coulomb energy, and the second refers to a unique functional of ρ, where [106]

$$G[\rho] \equiv T_s[\rho] + E_{xc}[\rho] \tag{7}$$

As previously stated, the functional comprises the kinetic energy of a non-interacting electron system together with the exchange and correlation energies, $E_{xc}[\rho]$, of an interacting system that yields the same electron density $\rho(r)$. Kohn-Sham theory alone is insufficient to formulate the functional. The strategy here will be to use an extension of the earlier discussed

Hartree product, the Hartree-Fock approximation, to where the Hartree product is replaced by a Slater determinant to enforce antisymmetry and incorporate exchange effects [107], and the Thomas-Fermi to eliminate the wavefunction entirely and formulate the problem directly in terms of the electron density, introducing a local approximation to the kinetic energy functional [108]. Using the local density to approximate the exchange-correlation functional is defined as the local density approximation (LDA) [109-111]. Among the many functionals, LDA is not as accurate as its successors involving gradient corrections. This works well for simple metals and systems with relatively homogeneous densities, but only as it overshoots the number of electron-electron interactions. The generalized gradient approximation (GGA) uses a more complex and, therefore, slower set of equations that delivers a greater precision [112]. By accounting for the local inhomogeneity and rate of change of the electron distribution through the density gradient, GGA effectively softens the overbinding of molecules and atoms seen in LDA [113]. This makes GGA functionals, such as the Perdew–Burke–Ernzerhof (PBE) functional, more accurate at describing the electronic properties of a wider variety of materials, including semiconductors, oxides, and surfaces. However, like LDA, it also underestimates band gaps and struggles with strongly correlated systems [114]. To address the issues presented, hybrid functionals, such as HSE06, attempt to resolve them by combining GGA and Hartree-Fock (HF) calculations [115, 116]. The inclusion of screened exact exchange in HSE06 significantly improves band-gap predictions over semi-local DFT functionals while maintaining a reasonable computational cost [117].

3.1.1.1 Hybrid Functionals (HSE06). In practical implementations of Kohn‑Sham DFT, the exchange‑correlation energy is described using approximate functionals. Consequently, semi-local functionals such as LDA and GGA often underestimate band gaps and cannot

accurately describe many excited-state properties. One prominent hybrid functional for solids was proposed by Heyd, Scuseria, and Ernzerhof (HSE) where the correlation energies, $E_{xc}[n]$, are defined as [117]

$$E_{xc}[\rho] = aE_x^{HF,SR} + (1-a)E_x^{PBE} + E_c^{PBE} \quad (8)$$

Correlates PBE rationale utilizing part of the exact exchange energy proposed by Perdew, which takes the form [114]

$$E_{xc}[\rho] = aE_x^{HF} + (1-a)E_x^{PBE} + E_c^{PBE} \quad (9)$$

where *a* is the mixing parameter and the HSE formalism, in contrast to Perdew, splits terms into short- and long-range components. Furthermore, the long-range term contributions are rather too small to consider, and calculating all Coulomb interactions in a hybrid functional is impractical.

As a result, HSE-type hybrid functionals provide a balanced and reliable description of electronic structure and are particularly successful in predicting band gaps. Nevertheless, exact exchange requires summations over all occupied bands and k-points and remains more computationally intensive than semi-local approaches, thereby demanding substantial high-performance computing resources [118, 119].

3.1.1.2 Wannier Functions. The free-electron gas has served as the foundational model for describing electrons in solids, since the electronic states of periodic systems are often conveniently represented using plane waves. An alternative perspective emphasizes that the nature of a solid is fundamentally a collection of atoms. Furthermore, it is natural to seek a description of the electronic structure that begins with atomic-like wave functions [120]. Wannier functions are spatially localized orbitals centered around atoms or chemical bonds.

The solution to the Kohn-Sham equations is constructed from the Bloch functions [121]

$$\psi_{nq}(r) = \frac{1}{\sqrt{N}} \sum_{R} w_n(R, r) e^{iq \cdot R} \tag{10}$$

where $w_{nR}(r)$ denotes the Wannier function, which depends on the relative distance of $r - R$, the exponential is a pure phase factor, and *N* is the number of lattice sites. If one should happen to know the Bloch functions, Wannier functions can be recovered as

$$w_n(R, r) = \frac{1}{\sqrt{N}} \sum_{q} \psi_{nq}(r) e^{-iq \cdot R} \tag{11}$$

This localization makes them valuable for analyzing chemical bonding, constructing tight-binding models, and efficiently interpolating DFT-derived band structures [122].

3.1.1.3 GW Approximation. An alternative approach for calculating electronic band structures and excitation energies is based on Green's function formalism. Unlike density functional theory (DFT), which relies on approximate exchange‑correlation functionals and is fundamentally a ground-state theory, Green's function methods provide a framework for describing electronic excitations in interacting many-body systems. The GW approximation, based on many-body perturbation theory, improves the DFT electronic structure by replacing the exchange‑correlation potential with a dynamic self-energy that accounts for electron‑electron interactions [123]. Experimentally, the electronic structure and quasiparticle excitation energies of a material can be investigated using photoemission spectroscopy. By measuring the kinetic energies of the emitted electrons, their binding energies and quasiparticle energy levels can be determined. With the one-particle Green's function,

$$G(r_{1,}t_{1;}r_{2,}t_{2,}) = -i\langle\psi_0|T[\psi(r_{1,}t_1)\psi^{\dagger}(r_{2,}t_{2,})]|\psi_0\rangle \tag{12}$$

where a time-ordered operator, T, acts on a product of Heisenberg field operators, ψ, to yield an order where time decreases from left to right [124]. This equation originates in the question of what the amplitude must be for a particle (or hole) at a point r_1 to propagate to r_2. For this, we obtain the ground state energy, the one-electron excitation spectrum, and an expectation value of a one-particle operator within the ground state. In the case of a two-particle system, our Green function would be defined as [125]

$$G(1,2,3,4) = -i \times -i\langle\psi_0|T[\psi(1)\psi(3)\psi^\dagger(2)\psi^\dagger(4)]|\psi_0\rangle \tag{13}$$

where the numerical labels $G(1,2,3,4)$ are shorthand for the full set of space, time, and spin coordinates associated with the field operators. The equation of motion for G generates higher-order Green's functions; to make it feasible, we use the Dyson equation [126]

$$G = G_0 + G_0 \sum G \tag{14}$$

where G_0 is a direct propagation from two points without exchange-correlation interactions, and the latter accounts for all possible exchange-correlation interactions from those two points. Similar Dyson-like equations exist for higher-order propagators like the Bethe-Salpeter equation, which is related to the two-body Green's function [127].

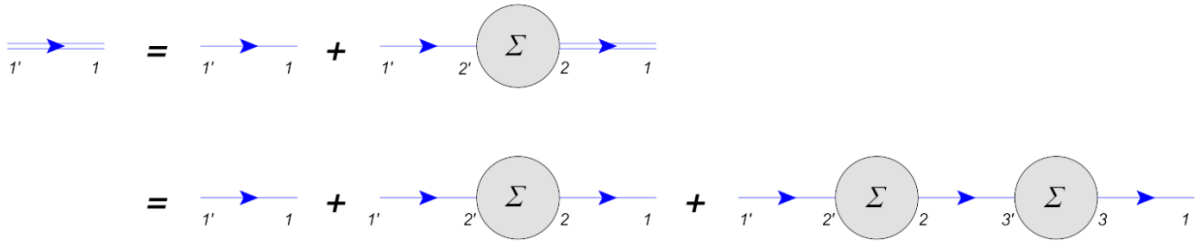

Figure 2: Dyson Equation representation of interacting Green's function. Note. Reprinted from [128].

Figure 2 shows a Feynman diagram interpretation of the foundational Dyson equation. The double line represents the probability amplitude of a particle (or hole) traveling from point

r_1 to propagate to r_2 as it interacts with its surrounding electronic environment; this is known as the interacting Green's function. This full propagator is mathematically composed of a non-interacting Green's function (the single line) bare trajectory of a particle moving between those two points completely alone, plus a self-energy building block Σ, that neatly condenses all complex correlation energies and many-body Coulomb collisions into a single, unified operator.

Because all the interaction effects are contained in the summation, GW, in a quantum fashion, uses four Dyson-like equations derived by Hedin to express the self-energy [129].

$$\sum = iGW \tag{15}$$

In practice, the formal structure of the GW approximation must be translated into a computational framework suitable for realistic materials. The self-energy is evaluated generally in reciprocal space and the frequency domain. Quasiparticle energies are obtained by perturbatively correcting the Kohn–Sham eigenvalues via a matrix element of the difference between the GW self-energy and the exchange–correlation potential [130]. Through this procedure, GW provides corrected band structures and excitation energies that explain many-body exchange–correlation effects beyond mean-field theory.

3.1.1.4 Bethe-Salpeter Equation (BSE). The Bethe–Salpeter Equation (BSE) can be viewed as a Dyson-like equation formulated for higher-order propagators. Whereas the Dyson equation relates the interacting and non-interacting one-particle Green's functions through the self-energy, the BSE introduces a two-particle correlation function, something like Eq. 11, which is defined as [131]

$$G(1,2,1',2') = \langle N,0 \left| T[\psi(1)\psi(2)\psi^{\dagger}(2')\psi^{\dagger}(1)] \right| N,0\rangle \tag{16}$$

Governing the correlated propagation of electron–hole pairs [132]. The motion of the two-particle Green's function obeys the BSE [131]

$$L(1,2;1',2') = G(1,2')G(2,1') + \int G(1,3)G(3,1')K(3,4';3',4)L(4,2;4',2')d(3,3',4,4') \quad (17)$$

where $L(1,2;1',2')$is the two-particle correlation function, and $K(3,4';3',4)$ is an electron-hole interaction kernel. This kernel plays a role analogous to the self-energy in the one-particle Dyson equation, but now at the level of two-body correlations. Consequently, the BSE incorporates excitonic effects and yields an accurate description of neutral excitations and optical response in interacting many-body systems.

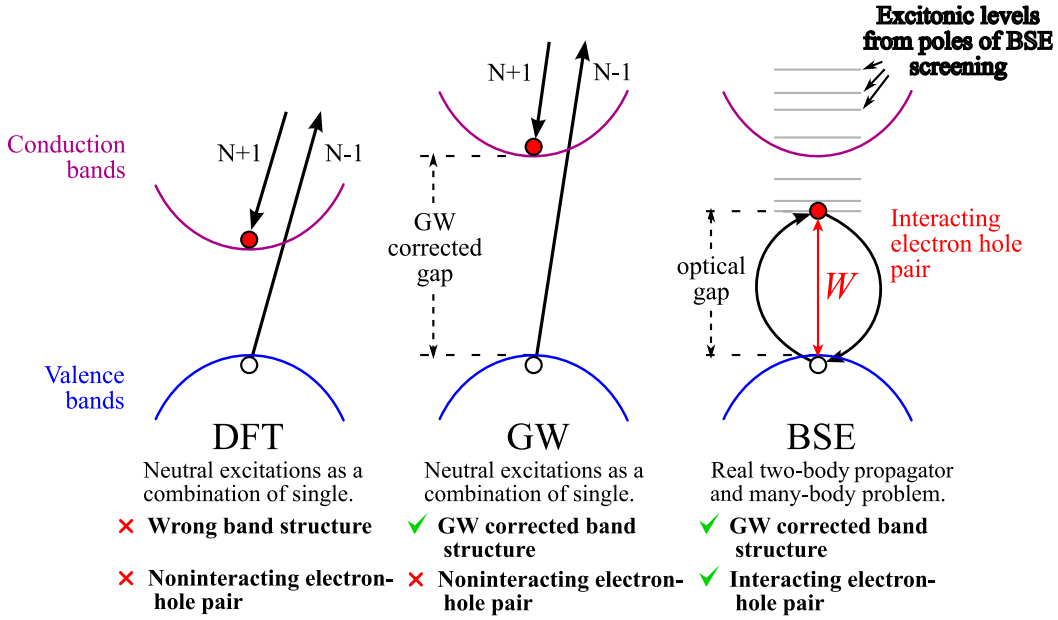

Figure 3: Optical spectra comparison between DFT, GW, and BSE. Note: Reprinted from "Bethe-Salpeter equation in ABINIT," by ABINIT Group, 2026, ABINIT Documentation. https://docs.abinit.org/theory/bse/.

Figure 3 illustrates the conceptual differences between DFT, GW, and BSE. In standard DFT, the electronic structure is described using Kohn–Sham single-particle energies, which often underestimate the band gap. The GW approximation improves upon DFT by replacing the

exchange–correlation potential with a quasiparticle self-energy that accounts for the screened Coulomb interaction between an added electron or hole and the surrounding electrons. This generally provides more accurate quasiparticle band gaps. Using these corrected GW energies, the Bethe–Salpeter equation (BSE) accounts for electron–hole interactions to describe excitonic effects and calculate optical excitation spectra.

3.1.2 Quantum Theory of Atoms in Molecules (QTAIM)

Through the Hohenberg-Kohn formalism, the total energy of a system is treated as a functional of its electron density, as previously established in the DFT subsection. Within this framework, Riess and Münch [133] provide a generalized parametrization of atomic near-transferability across different systems using a subdomain approach .The theory of atoms in molecules is based on generalizing a subsystem to the total system [134]. In other words, "are there atoms in molecules?" The generalization of a subsystem to the total system is only possible if [134]

$$\nabla\rho \cdot \hat{n} = 0 \tag{18}$$

where the subsystem is bounded by a surface ($\hat{n}$ is the unit vector normal to the surface) through which the flux in the gradient vector field of the charge density, $\nabla\rho$, is equal to zero. Thus, these gradient paths will render the interatomic surface boundary [135]. The Quantum Theory of Atoms in Molecules (QTAIM) uses topological analysis based on gradient paths to define chemical bonds, predict their multiplicity, and determine the boundaries of atoms within molecules [136].

QTAIM can be used to characterize the nature of a chemical bond via the adimensional ratio ($|V_b|/G_b$) at the bond critical point b, where V and G are the potential and the definite

kinetic energies, respectively [137]. Espinosa *et al*. [138] stated that for $||V_b|/G_b$>2 the interaction between two atoms is of a shared shell (i.e., covalent bonding), whereas for $|V_b|/G_b$>1 is of a closed shell.

3.1.3 Electron Localization Function (ELF) analysis

The Electron Localization Function (ELF) is used to understand and visualize the atomic shell structure, especially the pair electron localization [139]. It was originally described by Becke and Edgecombe [140] as $\eta(\vec{r}) = 1/(1 + \chi(\vec{r})^2)$, where $\chi(\vec{r})$ is the ELF kernel and $0 \leq \eta(\vec{r}) \leq 1$. The case of $\eta(\vec{r}) = 1$ corresponds to perfect localization, whereas $\eta(\vec{r}) = 0.5$ is the ELF for the electron gas.

In chemical bonding analysis, ELF provides a real-space description of how electrons are localized around atoms and between bonded atoms. High ELF values are typically associated with localized electron pairs, such as lone pairs, core electrons, or covalent bonding regions. In contrast, low ELF values indicate delocalized or depleted electron-density regions. Therefore, ELF is particularly useful for distinguishing between different bonding environments, including covalent, ionic, and metallic-like interactions. When combined with QTAIM analysis, ELF offers a more complete interpretation of bonding, charge localization, and the role of dopant atoms in modifying the electronic structure of the material.

3.2 Computational Modeling

3.2.1 Vienna Ab initio Simulation Package code

As DFT has become a powerful and widely used tool for studying material properties, a robust range of codes has emerged, including CASTEP, Quantum Espresso, Vienna *Ab initio*

Simulation Package (VASP), CRYSTAL, and Gaussian. Firstly, developed in 1986, CASTEP uses the plane-wave pseudopotential method to describe the behavior of electrons and nuclei in any situation [141]. The plane-wave pseudopotential method expands valence-electron wavefunctions in a simple plane-wave basis set while replacing the strong ionic potential and tightly bound core electrons with a smoother pseudopotential [142]. This approach reduces the number of basic functions needed, making DFT calculations efficient while retaining most of its accuracy regarding electron behavior. Furthermore, CASTEP offers a direct method for measuring physical properties such as structure, vibrations, and spectra. In contrast, experiments use indirect methods (x-ray or electron diffraction, neutron scattering) or probes (STM and AFM, ion scattering) to study such properties [143, 144].

Quantum Espresso is an open-source DFT code that owes its popularity to its numerous features regarding electronic-structure simulations [145, 146]. Furthermore, Quantum Espresso is more learner-friendly than the other software presented. However, Quantum Espresso has lagged in code development and requires immediate attention to maintain its large user base.

VASP is the most popular plane-wave pseudopotential method due to its high accuracy and excellent performance on high-performance computing clusters. The accuracy of DFT calculations depends on the choice of exchange-correlation functional [147]. VASP uses LDA for basic calculations, where, in the limit of uniform density, the exchange-correlation energy equals the exact energy of the uniform electron gas at that density. GGA is best for bulk materials and standard calculations. Accurate band gaps and systems with localized electrons are best for hybrid functionals. The VASP calculations presented here use GGA with the PBE functional for the band structure and density of states (DOS). This was also obtained using the

HSE06 hybrid functional. The kinetic energy cutoff for all calculations is 600 eV, which ensures the integrity of our results. The energy convergence criteria were set at 10^{-9} eV, and the geometry optimization criteria at 10^{-4} eV/Å per atom.

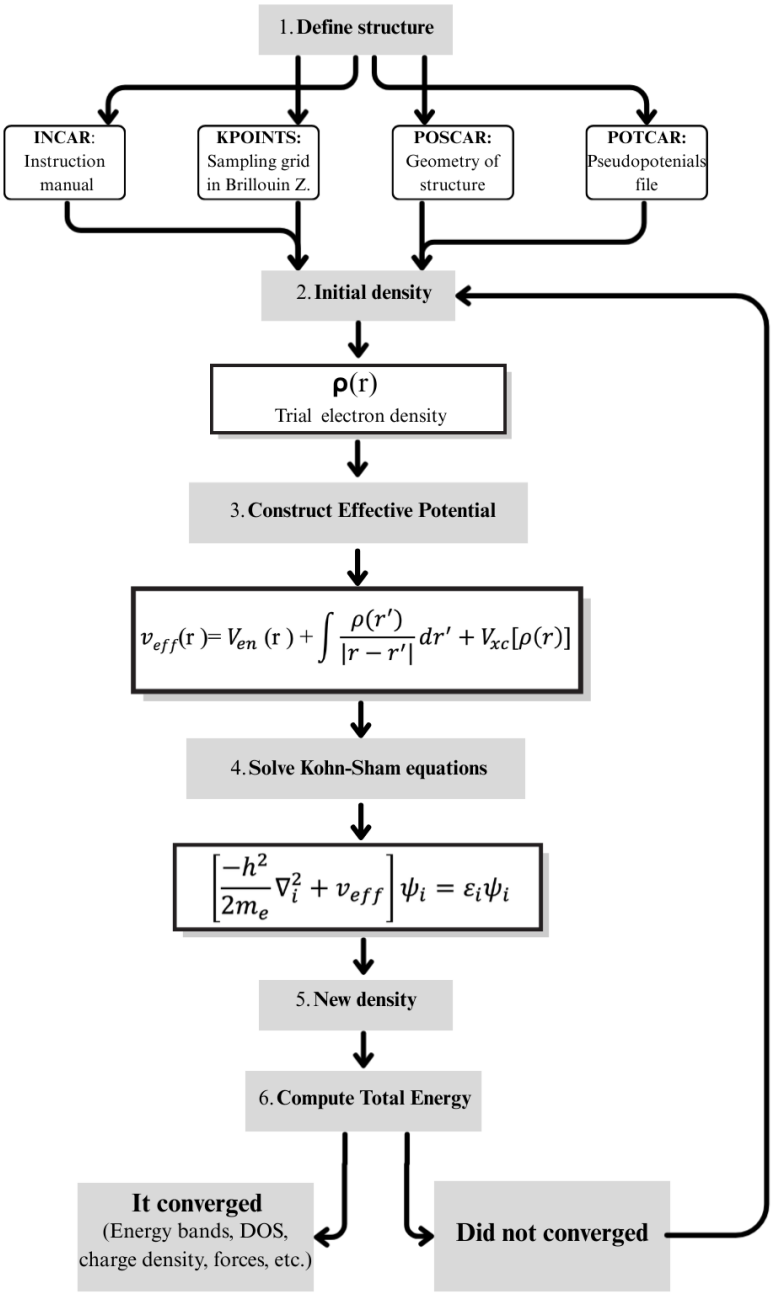

Figure 4: VASP-code schematic

3.3 Nano Powder Characterization

The following section examines the primary analytical instrumentation utilized for material characterization, with an emphasis on Thermogravimetric Analysis (TGA), X-Ray Diffraction (XRD), and Scanning Electron Microscopy (SEM).

3.3.1 Thermogravimetric Analyzer (TGA)

The thermogravimetric analysis was performed using the TA Instruments SDT Q600 TGA/DSC. The furnace features a horizontal dual-beam design that supports both a sample and a reference cup. The ceramic beams contain embedded thermocouples to measure sample, reference, and differential temperatures over the range from ambient to 1,500°C. The system uses a horizontal purge gas flow through the furnace and across the sample and can detect weight changes as small as 0.1 µg with a temperature sensitivity of 0.001°C. The TGA is used to study temperature-induced phenomena such as phase transitions and combustion.

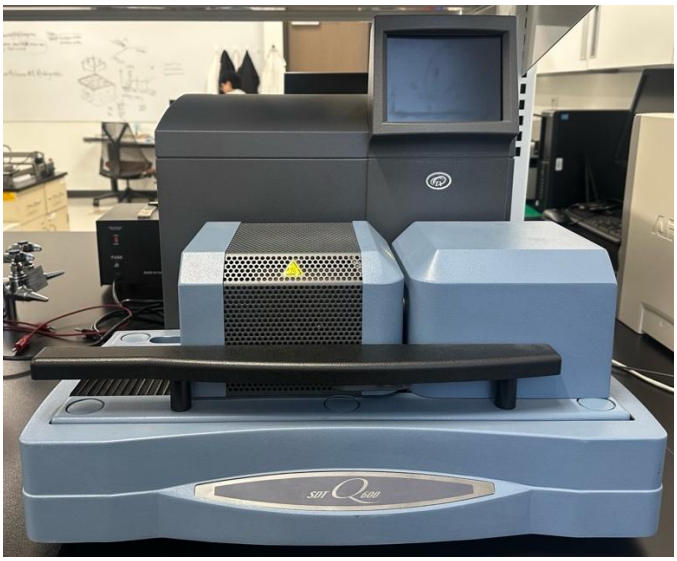

Figure 5: TA Instruments SDT Q600 TGA/DSC

For pure LT and its dopant configurations, all tests were performed in ambient air without additional purge gases, with a sample mass of 12 mg and a heating rate of 20.0°C/min from ambient temperature to 1100.00°C. For pure BN and the BN-Ag composites, tests were conducted either in ambient air or argon with a flow rate of 100 ml/min, with a sample mass of 12 mg and a heating rate of 20.0°C/min from room temperature to 1000.00°C.

3.3.2 X-Ray Diffraction (XRD)

XRD is an experimental characterization technique that determines the atomic and molecular structure of a crystalline material by analyzing the diffraction patterns produced when X-rays interact with the material [148]. The geometrical interpretation of XRD follows Bragg's law [149]

$$n\lambda = 2dsin\theta \tag{19}$$

n denotes the integer order of reflection, λ is the wavelength of the incident radiation, d represents the interplanar spacing of the scattering lattice planes, and θ is the angle of incidence. An X-Ray diffractogram displays characterization peaks coherent with Scherrer's equation [150]

$$D = \frac{K\lambda}{\beta cos\theta} \tag{20}$$

where D is the crystallite size, K is the dimensionless shape factor, λ is the wavelength of the incident X-rays, β the position of the XRD peak in radians, and θ the Bragg angle. All XRD analyses were performed using the Bruker D-2 Phaser. Data were collected with an angular step size of 0.02°, and the samples were rotated at 15 rpm during measurement to enhance particle statistics and improve signal averaging.

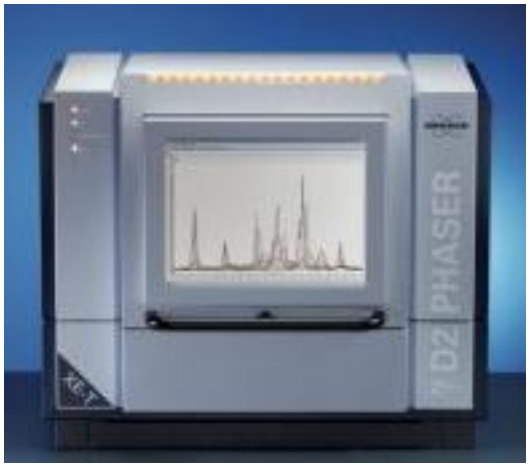

Figure 6: Bruker D2 Phaser 2nd Gen X-ray powder diffractometer

3.3.3 Scanning Electron Microscope (SEM)

The particle size distribution and surface morphology of the nanoparticles were characterized using Scanning Electron Microscopy (SEM). This technique provides high-resolution imaging of surface morphology at the nanoscale using a focused electron beam. The microscope is equipped with a motorized specimen stage to enable precise sample positioning and controlled imaging conditions. SEM analyses were performed using a JEOL JSM-7100F microscope; measurements were conducted at accelerating voltages typically ranging from 5 to 30 kV. Depending on the conductivity and dimensions of the sample. When necessary, samples were sputter-coated with gold using the JEOL Smart coater.

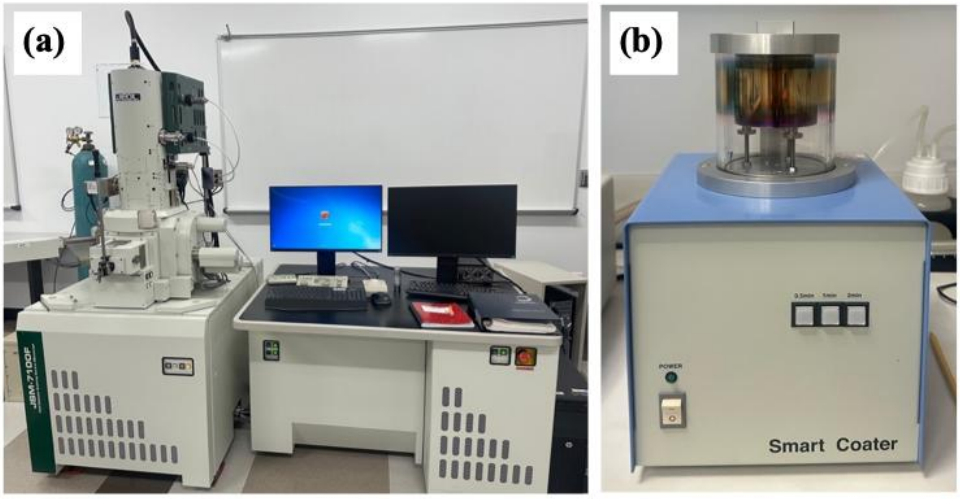

Figure 7: (a) JEOL JSM-7100F scanning electron microscope and (b) JEOL Smart coater

3.4 Additional Laboratory Equipment

This section provides a general overview of the additional laboratory equipment used in the experiments.

3.4.1 High-Energy Ball Mill

For powders of the materials to be mixed, a high-energy mill is used to vigorously shake the vial, colliding the powder mixture with the balls inside. Some parameters that have an effect on the powder, such as the type of grinding medium, milling time, type of mill, etc. [151]

Figure 8: High Energy 3D Ball Mill– MSK-SFM-3

The MSK-SFM-3 ball mill was used for mixing the wet media during sample preparation. As shown in Figure 8, the jar is supported by a disk that allows the media to shake and rotate at high frequencies. To minimize contamination, zirconium oxide balls were used as the milling media due to their high abrasion resistance [152]. A 4:1 ball-to-powder ratio (BPR) was used as only small-batch samples were prepared. The total milling time per mixing media is 5 minutes, as longer milling times will lead to undesirable phases and agglomeration due to temperature effects [153].

3.4.2 Hydrothermal Autoclave Reactor

Hydrothermal autoclave reactors are engineered to facilitate hydrothermal and solvothermal reactions under conditions of elevated pressure and temperature. The term "hydrothermal" specifically refers to the behavior of aqueous solutions under these extreme

parameters [154]. This synthesis method allows for precise control over a wide range of morphologies, enabling the chemical functionalization of desirable properties within 2D materials [155]. In this study, specifically through coupling with Ag to produce a nanocomposite. As illustrated in Figure 9, the autoclave assembly consists of two primary components: an outer high-quality stainless-steel jacket and an inner Polytetrafluoroethylene (PTFE) liner.

For Ag/*h*-BN nanocomposite synthesis, the hydrothermal autoclave reactor was set to a safe operating temperature of 160°C.

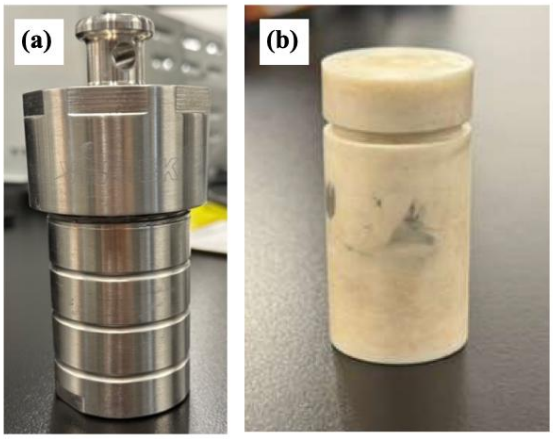

Figure 9: Hydrothermal Autoclave reactor (a) stainless-steel jacket and (b) PTFE vessel.

3.4.3 OSSILA Four- Probe Machine

The sheet resistance of the pellet was measured using the four-point probe method with an OSSILA four-point probe system, as displayed in Figure 10. This method was chosen to monitor changes in electrical resistance as an indicator of chemically resistive reactions in response to exposure of the BN/Ag pellet to gas.

Figure 10: OSSILA four- probe machine

3.4.4 Spark Plasma Sintering (SPS) Machine

Spark Plasma Sintering (SPS) rapidly consolidates powder using direct electrical current under low atmospheric pressure. SPS enhances the mechanical, thermal, and electrical properties of the powder [156]. To minimize porosity, prevent oxidation, and maximize mechanical strength, the *h*-BN-30wt.% Ag powder was consolidated via spark plasma sintering at 700°C and 50 MPa under a nitrogen atmosphere.

Figure 11: Spark Plasma Sintering System

CHAPTER IV

UNDOPED AND ER-DOPED LITHIUM TANTALATE

This chapter presents a comprehensive computational and experimental study of undoped and Er^{3+}-doped LT. The theoretical parametrization, material synthesis, and key findings are discussed in detail. The data presented here have been previously published in [157].

4.1 Calculation Parameters

The following discussion outlines the specific parameters used to simulate the electronic structures and optical response functions for pure LT and Er^{3+}-doped LT.

4.1.1 Supercell modeling

Figure 12 shows the DFT-optimized LT 2×2×1 supercell in a triclinic form (space group R3c) with 24 Li, 24 Ta, and 72 O atoms (120 atoms in total). Each Li and Ta atom is coordinated with six oxygens in an octahedral symmetry. This supercell is used for both the LT and 4.167 % Er^{3+}-doped LT configurations.

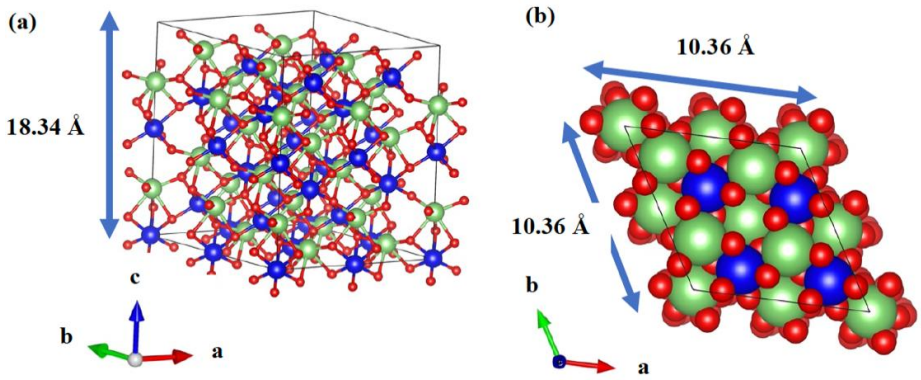

Figure 12: (a) The side view of the $LiTaO_3$ (LT) optimized 2×2×1 supercell and (b) its top view. Atoms are colored as follows: Li, green; Ta, blue; O, red. The thin lines denote the unit cell boundaries. Note. Reprinted from [157].

4.1.2 Density Functional Theory Parameters

DFT electronic structure calculations, optimal geometries, and the dielectric functions were obtained for the LT host and its Er^{3+}-doped counterparts using the periodic code VASP and the projector augmented-wave (PAW) pseudopotentials. The Kohn-Sham equations were solved with the GGA PBE functional and the HSE06 hybrid functional to obtain the corrected band structure and DOS.

The kinetic energy cutoff for all calculations is 600 eV, which ensures the integrity of our results. The energy convergence criteria were set at 10^{-9} eV, and the geometry optimization criteria at 10^{-4} eV/Å per atom. The Brillouin zone was sampled using the Γ-centered 6×6×6 grid.

4.2 Sample Preparation

4.2.1 Tantalum Oxide (Ta_2O_5) preparation

Commercially sold Tantalum Oxide (Ta_2O_5) consists of a heterogeneous mixture of micro- and nanometer-sized particles. To improve sample homogeneity, Ta_2O_5 was converted via chemical precipitation to obtain particles predominantly in the nanometer size range. This top-down process is described in Ref. [158], where Ta_2O_5 is first dissolved in an HF solution to form

Tantalum Fluoride (TaF). This is later neutralized, leading to the precipitation of tantalum oxide precursors that, upon washing and drying, yield nanoscale Ta_2O_5 particles.

$$Ta_2O_5 + 10\,HF \rightarrow 2TaF_5 + 5H_2O \quad (21)$$

$$2TaF_5 + 10NH_4OH \rightarrow Ta_2O_5 + 5H_2O + 10NH_4F \quad (22)$$

In this method, a single batch consists of 0.28 g of Ta_2O_5 dissolved in 5 mL of 48% HF in a water bath at 75°C for 8 hours. Afterward, it was neutralized by a 30% solution of Ammonium Hydroxide (NH_4OH), washed three times with deionized water, centrifuged, and dried at 100ºC for 12 hours. The powder characterization of Ta_2O_5 nanoparticles is discussed later in this chapter.

4.2.2 Pure and Erbium-doped Lithium Tantalate (LT) preparation

To synthesize pure and Er^{3+}-doped LT nanoparticles, the prepared Ta_2O_5 nanoparticles were mixed with a stochiometric amount of lithium hydroxide (LiOH) and varying concentrations (0.5–10 mol.%) of erbium oxide (Er_2O_3).

$$pure\ LT \rightarrow Ta_2O_5 + 2LiOH \rightarrow 2LiTaO_3 + H_2O \quad (23)$$

$$Er - doped\ LT \rightarrow LiTaO_3 + (0.5 - 10\ mol.\%)Er_2O_3 \rightarrow LiTaO_3 - (0.5 - 10\ mol.\%)Er \quad (24)$$

For pure LT, 0.55 g of Ta_2O_5 and 0.057g of LiOH are mixed in acetone with zirconia balls in a high-energy ball mill for 5 minutes. The resulting mixture was subsequently air-dried and then heat-treated in an oven at 650°C for 4 hours.

For a 0.5g mixture in the 0.5 mol% Er^{3+}-doped LT case, 0.449 g of Ta_2O_5, 0.049 g of LiOH, and 0.002 g of Er_2O_3 are mixed in acetone with zirconia balls in a high-energy ball mill for 5 minutes. The resulting mixture was subsequently air-dried and then heat-treated in an oven

at 650°C for 4 hours. For all doping configurations, the required dopant concentrations were adjusted accordingly.

4.3 Results and Discussion

4.3.1 Tantalum Oxide powder characterization

As previously noted, commercially available Tantalum Oxide (Ta_2O_5) consists of a heterogeneous mixture of micro- and nanometer-sized particles. SEM and XRD characterizations were conducted to verify the total conversion of the Ta_2O_5 precursor and the uniformity of the resulting nanostructure.

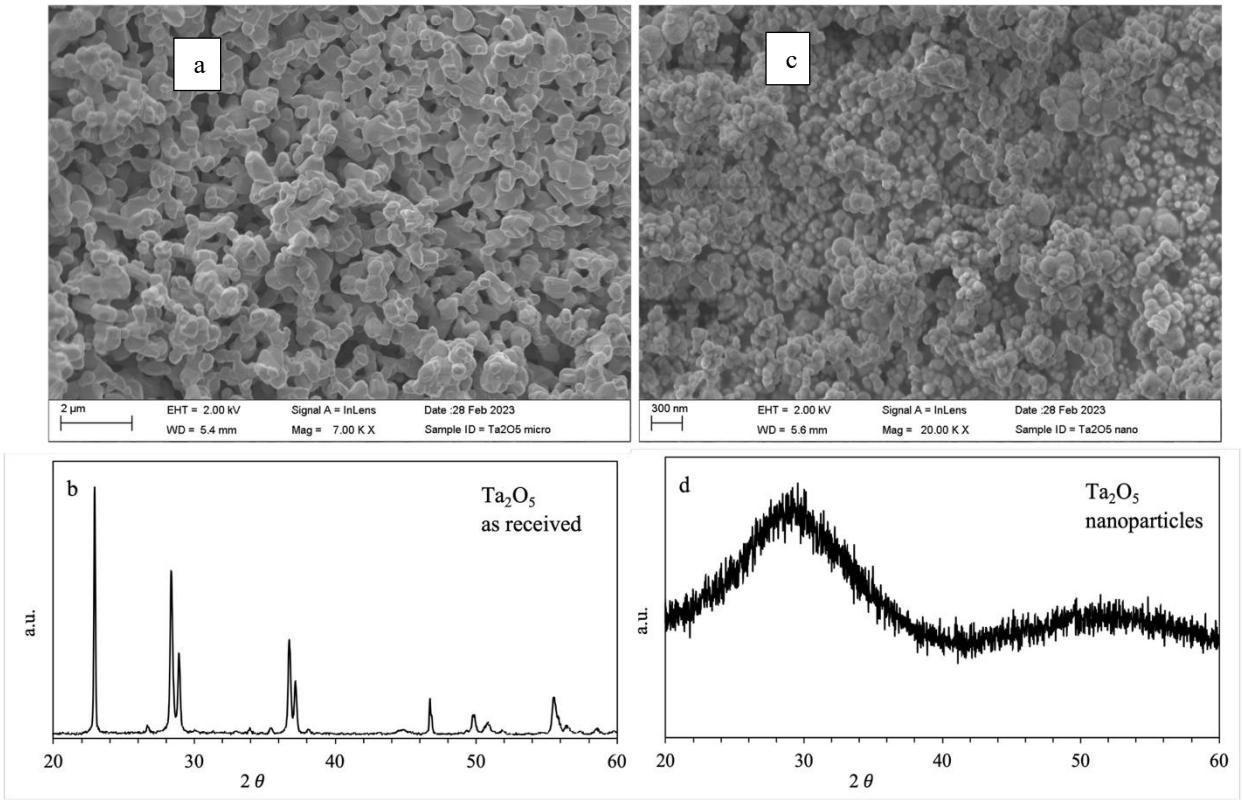

Figure 13:Top. SEM analysis of (a) commercially sold Ta_2O_5 and (c) transformed Ta_2O_5 nanoparticles. Bottom. XRD analysis of (b) commercially sold Ta_2O_5 and (d) transformed Ta_2O_5 nanoparticles.

Figure 13 (left) illustrates the XRD peaks of the as-received Ta_2O_5 and their corresponding SEM images. The powder exhibits a predominantly micron-sized morphology and distinctive characterization peaks corresponding to well-crystallized powder. Figure 13 (right) depicts a significant reduction in scale, with an average particle size below 100 nm. The XRD analysis of the transformed Ta_2O_5 shows a higher peak count and an amorphous hump, confirming a reduction in crystallite size and successful nanoparticle synthesis.

4.3.2 DSC/TGA analysis

The DSC/TGA thermogram is a graphical representation of the decomposition of a material as temperature changes over time. Thermal events appear in the thermogram as a series of peaks corresponding to energy release (exothermic processes) and troughs corresponding to energy absorption (endothermic processes). The interplay of these thermal phenomena offers insight into the material's structural characteristics and stability.

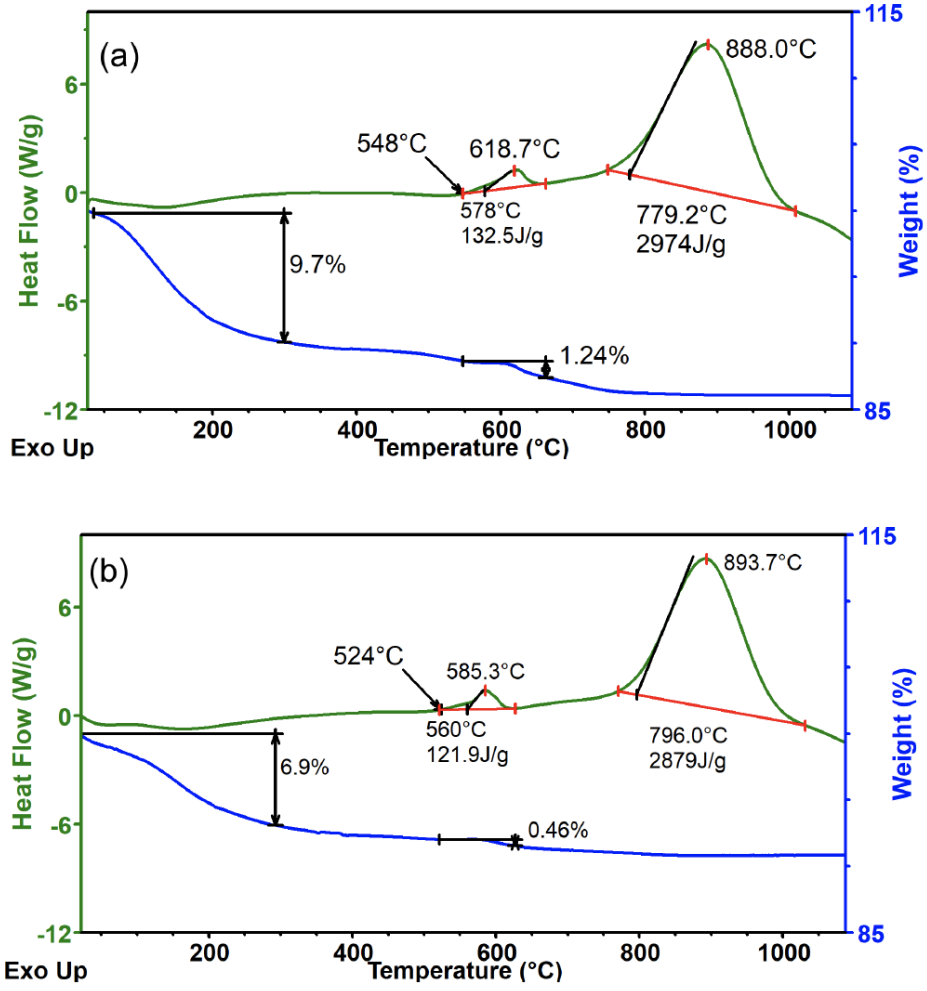

Figure 14: DSC/TGA analysis of (a) pure LiOH- Ta_2O_5 and b) LiOH- Ta_2O_5-3 mol% Er_2O_3. Note. Reprinted from [157].

For pure LT, Figure 14a displays a slight endothermic event accompanied by a weight loss of 9.7%, attributed to the evaporation of remnant solvents and water from the transformed Ta_2O_5. An initial exothermic reaction of 132.5 J/g occurs at 548°C with a corresponding weight loss of 1.24 %, which is attributed to the reaction between LiOH and Ta_2O_5. This result is significant, as it indicates that LT formation can be achieved at temperatures as low as 650°C.

Recrystallization is a thermally induced process in which the emergence of strain-free grains replaces deformed grains without altering the chemical composition of the material. This transformation is driven by a reduction in the internal energy of a material and is often accompanied by a rejection/release of heat from the material, which occurs around 790°C.

For LT-3 mol% Er^{3+}-doped, Figure 8b shows an endothermic reaction with a corresponding weight loss of 6.9%. An initial exothermic reaction of 121.9 J/g occurs at a reduced temperature of 524°C, with a corresponding weight loss of 0.46%, followed by recrystallization at 796°C. Overall, both DSC analyses indicate that the addition of Er^{3+} does not alter the thermal behavior of the material and that all LT compositions can be annealed at 650°C.

4.3.3 XRD and SEM analysis of Pure and Erbium-doped Lithium Tantalate

One of the primary objectives is to obtain LT nanoparticles; accordingly, XRD and SEM analyses were conducted to study the morphology and crystallographic structure of the prepared material.

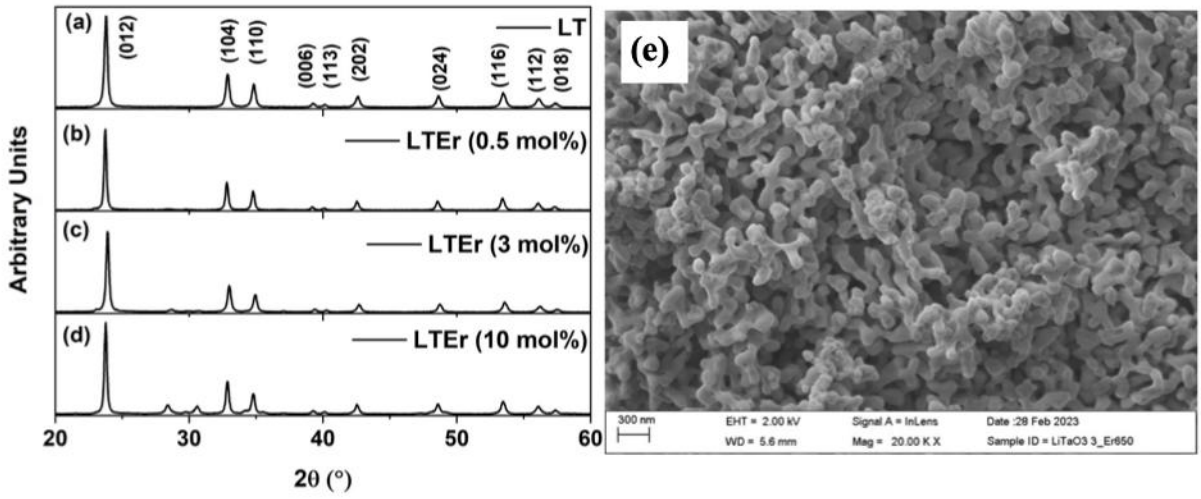

Figure 15: XRD analysis of (a) pure LT and (b, c, d) various configurations of Er^{3+}-doped LT and (e) SEM analysis of 3 mol.% Er^{3+}-LT. Note. Reprinted from [157].

Figure 15 (left) shows the XRD peaks for LT and for erbium-doped samples at three concentrations (0.5, 3, and 10 mol%). At higher Er^{3+} concentrations, additional peaks corresponding to Er_2O_3 appear around $2\theta = 30°$, indicating the presence of excess Er_2O_3. Nevertheless, erbium incorporation does not significantly alter the overall crystallographic structure of LT, regardless of whether Er^{3+} occupies lithium or tantalum lattice sites. Figure 15 (right) further confirms that the resulting material retains its nanoscale morphology.

4.3.4 Pure and Er^{3+}-doped LT band structure and DOS

In the previous chapter, the discussion primarily focused on how to calculate electronic band structures and obtain their corresponding/corrected band gaps through different codes. Moreover, it is also important to provide a brief overview of the fundamental concepts underlying electronic band structures, as they form the basis for understanding the electronic properties of materials.

A solid might be thought of as a compilation of independent atoms brought together and bonded to form the ordered arrangement that a crystal lattice carries. At large distances, each atom behaves as an isolated system with discrete energy levels. However, as atoms get closer, electrons are perturbed by the periodic potential of their neighboring atoms. From the standpoint of the Schrödinger equation, this perturbation can cause the discrete atomic states to potentially split and broaden into a continuum of allowed energies. As previously mentioned, in the Kohn-Sham framework, this effect is captured by the effective periodic potential and solved in terms of Bloch functions, where the atomic orbitals evolve into energy bands. The lower-energy bonding states become occupied, forming the valence band, while higher-energy, unoccupied states form the conduction band [159]. The energy difference between the highest occupied and lowest

unoccupied molecular orbital defines the band gap, which is key when determining the electrical conductivity of a material . Implementing dopants serves to reduce the bandgap.

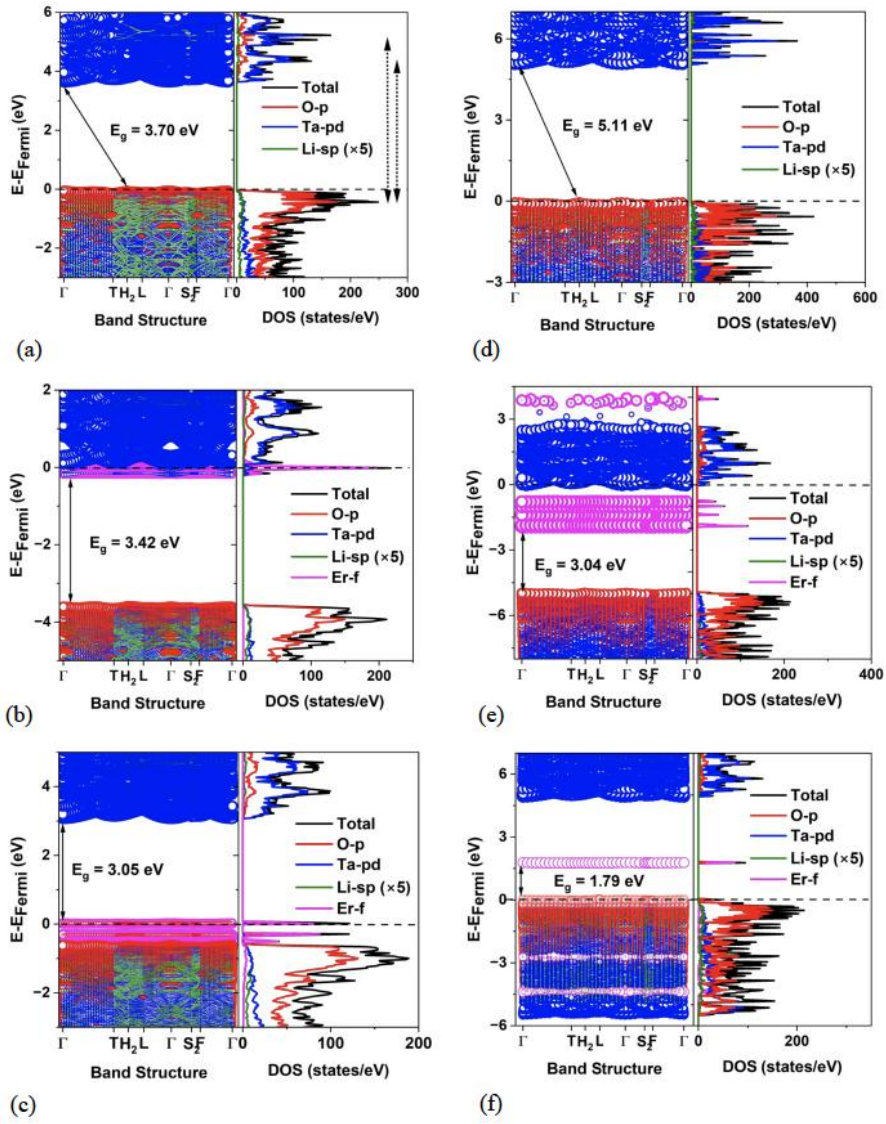

Figure 16: Electronic band structure with orbital projections using the Brillouin zone path and the corresponding total and projected DOS per orbital using the PBE calculations for all configurations of LT. (a) LT, (b) LT: Er^{3+} (4.167% Er^{3+}) with Er to substitute Li, and (c) with Er^{3+} to substitute Ta. (d), (e), and (f) show the corresponding HSE06 calculations for (a), (b), and (c), respectively. Note. Reprinted from [157]. In this dissertation, the ion notation is written as X^{3+} to be consistent with standard chemical notation, whereas the original published figure used X^{+3}.

Figure 16 presents the calculated electronic band structure and density of states (DOS) for LT and Er^{3+}-doped LT using both the GGA and HSE06 (hybrid) functionals. For pure LT, both calculations show similar profiles with lithium-derived states primarily contributing to the valence band and tantalum-derived states dominating the conduction band. However, the hybrid functional yields a significantly larger band gap of 5.11 eV than the 3.70 eV obtained with GGA.

The density of states (DOS) describes the number of available electronic states at each energy level and provides the true electronic structure of a material [160]. For pure LT, the DOS indicates that the O-p orbitals dominate at the valence band top, whereas the conduction band is dominated by Ta-pd orbitals. The small overlap between Li and O orbitals, compared to the stronger Ta–O hybridization, suggests that Li–O bonds are weaker than Ta–O bonds. This is consistent with the larger Li–O interatomic distances relative to those of Ta–O.

For both LT: Er^{3+} configurations using GGA, the DOS and band structure reveal Er^{3+}-4f bands near the Fermi level. When Er^{3+} replaces a Li site, the Er^{3+}-4f bands span approximately 0.2 eV, with an associated band gap of 3.42 eV. In contrast, hybrid functional calculations show a clear splitting of these f-states, which shift away from the Fermi level and appear at lower energies between -0.8 eV and -1.95 eV. As well as an unoccupied band around 3.8 eV. When Er^{3+} replaces a Ta site, the Er^{3+}-4f bands span the valence band top, with an associated band gap of 3.05 eV. In contrast, hybrid functional calculations show a clear splitting of these f-states at 1.76 eV, -2.83 eV, and -4.38 eV relative to the Fermi energy.

4.3.5 Pure LT and Er^{3+}-doped optical properties

The ultimate basis for understanding the dielectric behavior lies in the electrical nature of matter. The main effect of incoming light is to make electrons oscillate where their response is

caused by the neighboring electrons within a lattice. This is explained by the frequency-dependent dielectric function [161]

$$\varepsilon(\omega) = \varepsilon_R(\omega) + i\varepsilon_I(\omega) \tag{22}$$

Where $\varepsilon_R(\omega)$ and $\varepsilon_I(\omega)$ are its real and imaginary parts, respectively, and ω is the photon energy. This stems from a formulation of Maxwell's equations that describes not only the interaction of light with solids but also tracks the interactions between electrons and phonons [126]. External charges control the system, while internal charges respond. In the presence of an external field, Coulomb forces rearrange charges within a material in an attempt to achieve electrostatic equilibrium [162]

$$E(r) = \rho(r) = 0 \tag{23}$$

*w*here in a perfect conductor, the electric field and charge density vanish everywhere in the interior. The total charge density has two components [163]:

$$\rho(r) = \rho_{ext} + \rho_{pol} \tag{24}$$

A spatially varying polarization, ρ_{pol}, defined by the internal current that flows due to the external charges, ρ_{ext}. This changes Gauss's law to [163]

$$\nabla \cdot E(r,t) = 4\pi\rho(r,t) = 4\pi[\rho_{ext}(r,t) - \rho_{pol}(r,t)]$$

The rearrangement of terms defines the electric displacement as

$$D = E + 4\pi P = \varepsilon E \tag{25}$$

Where ε is the dielectric constant, a constant of proportionality between displacement and dielectric fields, which gives rise to the frequency-dependent dielectric function. The refractive index, *n* , and the extinction coefficient, *k*, are closely related to the dielectric function [164].

$$n(w) = \left(\frac{\varepsilon_R(w) + [\varepsilon_R^2 + \varepsilon_I^2]^{\frac{1}{2}}}{2} \right)^{\frac{1}{2}} \tag{26}$$

$$k(w) = \left(\frac{-\varepsilon_R(w) + [\varepsilon_R^2 + \varepsilon_I^2]^{\frac{1}{2}}}{2} \right)^{\frac{1}{2}} \tag{27}$$

The reflectivity depends on both *n* and *k* and is given by [165]

$$R = \frac{(n-1)^2 + k^2}{(n+1)^2 + k^2} \tag{28}$$

Building on this framework, we have investigated the microscopic origins of optical phenomena that arise as light travels through solid materials. Experimentally measurable quantities, such as the optical absorption coefficient and the imaginary part of the dielectric function, can be used to determine the dispersion of a material and the real part of the dielectric function through the Kramers–Kronig relations [166].

Figure 17 shows the optical properties are calculated using GGA for LT and Er^{3+}-doped LT with Er^{3+} substituting Li and Ta atoms. Figure 10a. denotes ε_I for all configurations of LT and their corresponding transitions from the valence to the conduction bands. For pure LT, the onset value is 3.6 eV, which corresponds to the electronic bandgap shown in Figure 16a. The dielectric constant ($\varepsilon_R(0)$), which is related to an integral overall dissipative process, is 4.9. Pure LT has a

refractive index $n(0)$ of 2.24 and a reflectivity of 15%. All values increase with the implementation of Er^{3+} atoms.

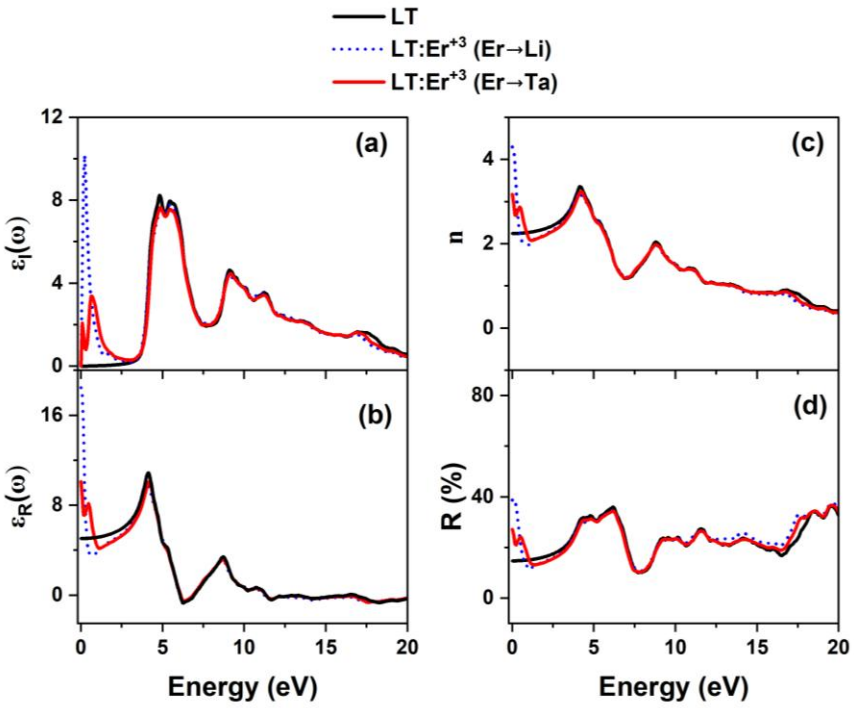

Figure 17: a) The imaginary part of dielectric functions ε_I for LT and its Er^{3+} doped counterparts for Er substituting Li ($Er^{3+} \rightarrow Li$) and Ta ($Er^{3+} \rightarrow Ta$), and b) the real part ε_R, c) the refractive index n, and d) the reflectivity R. Note. Reprinted from [157]. In this dissertation, the ion notation is written as X^{3+} to be consistent with standard chemical notation, whereas the original published figure used X^{+3}.

In both cases, the imaginary part of the dielectric function for Er^{3+}-doped LT exhibits distinct peak characteristics within the fundamental bandgap region. These spectral features correspond to electronic transitions within the Er^{3+} 4f manifold (intraband f–f transitions) and to interband transitions involving Er^{3+} 4f orbitals with states at the valence band maximum and conduction band minimum, consistent with previous findings. Intraband transitions within the same band, as for transitions from the valence to the conduction band, are referred to as interband transitions. Furthermore, for Er^{3+} substituting at the Li site, the DOS shown in Figure

16b indicates the presence of additional vacancies, leading to higher values of the optical coefficients.

The dielectric constant of the doped configurations is higher than that of pure LT, supporting the conclusion that Er^{3+}-doped LT is a superior dielectric material. The refractive index and reflectivity of Er^{3+}-doped LT are larger than those of pure LT for energies below approximately 0.9 eV, which correspond to infrared and longer wavelengths.

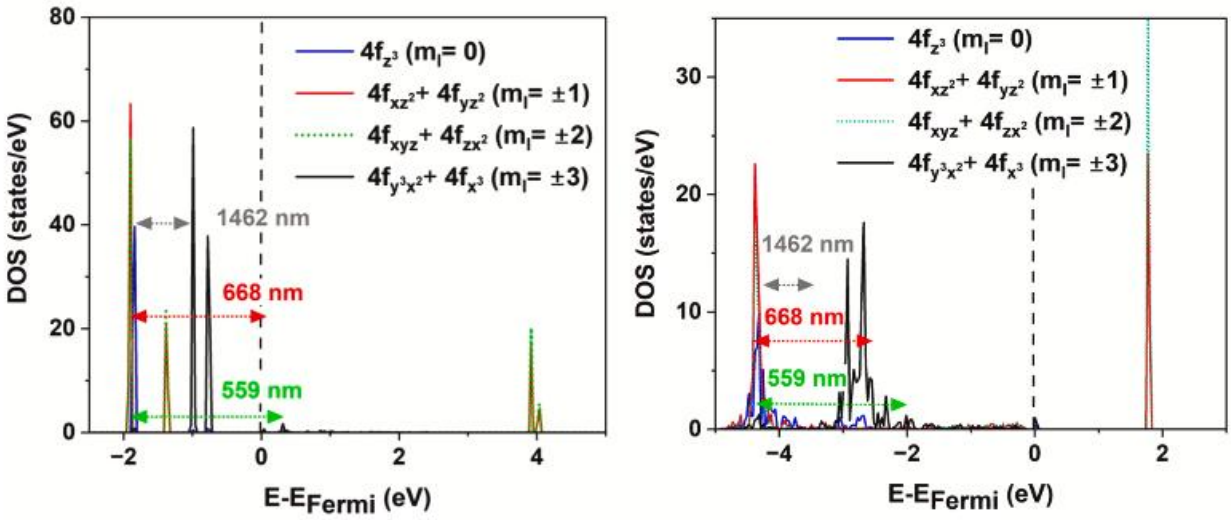

Figure 18: The DFT calculated Er^{3+}-4 f DOS using the HSE06 functional for Er^{3+}- doped LT when (left) Er substitutes a Li site and (right) at a Ta site. Note. Reprinted from [157].

Figure 18. shows DFT calculated Er^{3+}-4 f DOS using the HSE06 functional for Er^{3+}-doped LT when (left) Er^{3+}substitutes a Li site and (right) at a Ta site. The HSE06 reveals that both doping configurations feature Er^{3+}-4f states spanning above and below the Fermi level, indicating that they are partially filled. In the case of LT: Er^{3+}, when Er^{3+} replaces a Li site, minor hybridization of the Er-4f with the host conduction band occurs due to the splitting of these f-bands about -0.8 eV, -1.95 eV, and 3.80 eV relative to the Fermi level. The significant

mixing of the Er^{3+}-4f states is from the LT: Er^{3+} configuration when Er^{3+} replaces a Ta site. The broadening of the Er^{3+}-4f states below the Fermi energy agrees with the broadening of the imaginary part of the dielectric function, which allows for more f–f transitions to occur. The identified Er^{3+} f–f transitions from the HSE06 calculations correspond to the following wavelengths: 559 nm, 668 nm, and 1462 nm.

4.3.6 Pure and Erbium-doped photoluminescence analysis

Intuitively, physically recognizable effects are the consequence of a series of interacting microscopic events. To experimentally study the electronic excitation of a material, one performs photoemission analysis. Based on the previously calculated dielectric coefficients, Er^{3+}-doped LT is classified as a superior dielectric and is expected to be active at infrared wavelengths.

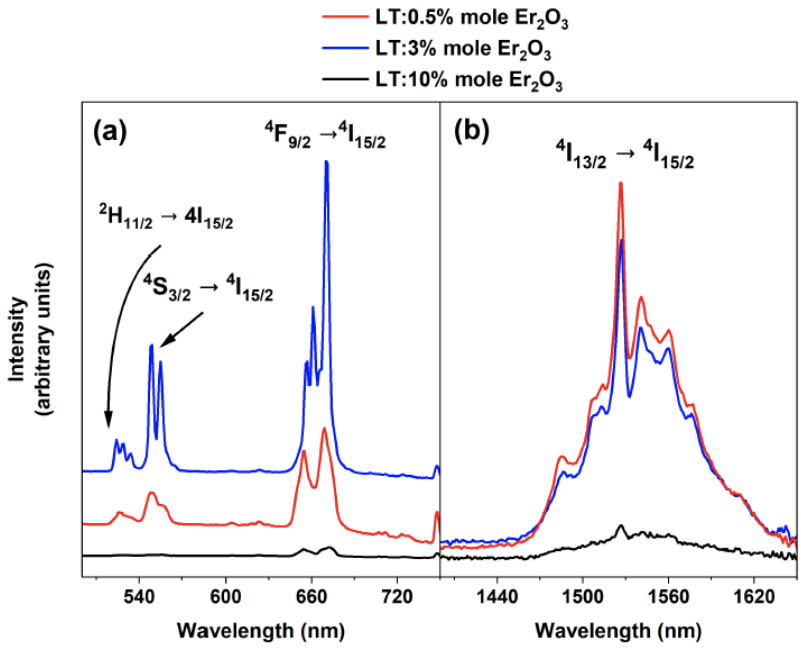

Figure 19: (a) The fluorescence emission spectra for LT: Er^{3+} under 0.5, 3, and 10 mol% of Er_2O_3 with the Er^{3+} transition assignments in the visible region and (b) the near IR. Note. Reprinted from [157].

As shown in Figure 19, the 3 mol% Er^{3+}-doped LT configuration exhibited the strongest photoluminescence emissions at 521–540 nm, 540–566 nm, and 645–689 nm, all of which fall within the visible spectrum. In contrast, within the 1454–1462 nm infrared region, the 0.5 mol% Er^{3+}-doped LT configuration exhibited slightly higher emission intensities than the 3 mol% Er^{3+}-doped LT configuration. The 10 mol% Er^{3+}-doped LT configuration shows weak emission in the visible and infrared regions compared with other doping configurations due to concentration quenching, in which rare-earth luminescence decreases with increasing dopant concentration [167-169]. Lastly, our computational and experimental results agree.

All these peaks are assigned to Er^{3+} f–f transitions. Neutral erbium has an electronic configuration of [Xe]$4f^{12}6s^{2}$, and Er^{3+} has an electron configuration of [Xe]$4f^{11}$ as it loses three electrons. With 11 electrons within the 4f subshell and an angular momentum quantum number (l) assignment of 3, each f-electron can have a magnetic quantum number (m_l) assignment of the following: -3, -2, -1, 0, 1, 2, and 3. In accordance with Hund's rules, which help determine the total spin (S), total spatial angular quantum momentum (L), and the total angular momentum of the ground state (J), the first and second postulates state that among the many-electron states arising from the same configuration, the ground state will have the largest total spin. Thus, the ground state must be the one with the highest angular momentum quantum number for this to be true [170].

Furthermore, to maximize L, m_l is maximized when m_l assignments 1, 2, and 3 are summed together to a value of L = 6, corresponding to a state I. As previously mentioned, Er^{3+} has an electron configuration of [Xe]$4f^{11}$ and has three unpaired electrons. Moreover, the shell is more than half full, so the ground state is represented as J = L + S. With an L of 6 and an S value

of 3/2 (three unpaired electrons), then J is equivalent to 15/2. Lastly, the spectroscopic notation for the initial $^4I_{15/2}$ state serves as the starting point for these electronic excitations.

CHAPTER V

Pr^{3+}/Er^{3+}-CO-DOPED LITHIUM TANTALATE

This chapter presents a comprehensive computational and experimental study of Pr^{3+}- and Pr^{3+}/Er^{3+}-co-doped LT. The theoretical parametrization, material synthesis, and key findings are discussed in detail. The data presented here have been previously published in [171].

5.1 Calculation Parameters

5.1.1 Supercell modeling

The supercell in Figure 20 shows the DFT-optimized LT 2×2×1 supercell in a triclinic form (space group R3c) with 24 Li, 24 Ta, and 72 O atoms (120 atoms in total). In the doped configurations, the Er^{3+} and Pr^{3+} atoms occupy either the Li or the Ta site, whereas, for the Pr^{3+}/Er^{3+}-co-doped configuration, both dopants occupy Li sites. The supercells were optimized using the lanthanides' 4f orbitals in the core.

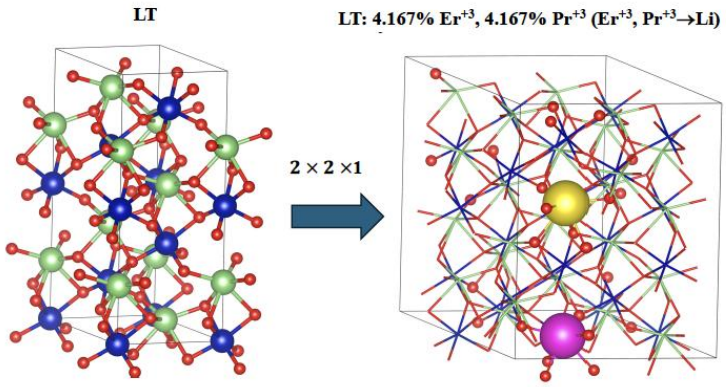

Figure 20: Left. The $LiTaO_3$ (LT) unit cell. Right. The 2×2×1 supercell of the LT: 4.167% Er^{3+}, 4.167% Pr^{3+} with $Pr^{3+}$and Er^{3+}at the Li site (Er^{3+}, Pr^{3+}→ Li). Atoms are colors as follows: Li, green; Ta, blue; Pr^{3+}, yellow; Er^{3+}, magenta; O, red. The thin black lines denote the supercell boundaries. Note. Reprinted from [171]. In this dissertation, the ion notation is written as X^{3+} to be consistent with standard chemical notation, whereas the original published figure used X^{+3}.

5.1.2 Computational Parameters

DFT electronic structure calculations, optimal geometries, and the dielectric functions were obtained for the LT host and its Er^{3+}- and Pr^{3+}-doped and co-doped counterparts using the periodic code VASP and the projector augmented-wave (PAW) pseudopotentials. The Kohn-Sham equations were solved using the PBE functional within GGA and the HSE06 hybrid functional to obtain the corrected band structure and DOS.

The kinetic energy cutoff for all calculations is 600 eV, which ensures the integrity of our results. The energy convergence criteria were set at 10^{-9} eV, and the geometry optimization criteria at 10^{-4} eV/Å per atom. The Brillouin zone was sampled using the Γ-centered 6×6×6 grid. QTAIM and ELF are calculated using the Critic2 code, which reads VASP output. Figure 21a. shows the QTAIM molecular graph for the LT:4.176% Er^{3+}, 4.176% Pr^{3+}, which is a collection of density trajectories originating at the (3, -1) bond critical points and connecting the electron density critical point maxima (3, -3) with other maxima. Figure 21b. shows the negative of the Laplacian of the

electron density at the (001) plane at the Pr^{3+} c-axis location, and Figure 21c. shows the contour plot of electron density along the plane defined by Er^{3+} and two nearby O atoms, as well as the atomic basins and the trajectories. The atomic basins are regions of space traversed by density and bounded by zero-flux surfaces.

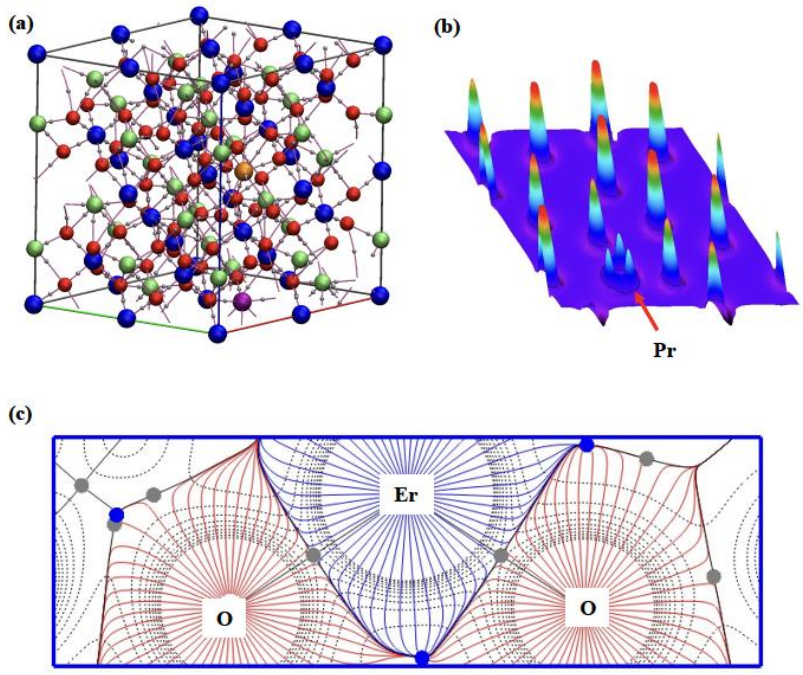

Figure 21 (a) The molecular graph of the electron density for the optimized LT:4.176% Er^{3+}, 4.176% Pr^{3+} supercell using VMD and critic2. Only the (3, -1) bond critical points are shown. Atoms are colors as follows: Ta, blue; O, red; Li, green; Er^{3+}, purple; Pr^{3+}, orange. Small gray spheres show bond critical points. (b) The negative of the Laplacian of the electron density $-\nabla^2\rho(\vec{r})$ at the (0 0 1) plane, which includes the Pr^{3+} atom, whereas the remaining peaks are from oxygens generated via AIM-UC. (c) The contour plot of the electron density along the plane defined by Er^{3+} and two nearby O atoms. Blue and gray circles represent (3, +3) and (3, -1) critical points, respectively. The trajectories are blue and red for the Er^{3+} and O basins, respectively. Note. Reprinted from [171].

5.2 Sample Preparation

Similarly to Er^{3+}-doped LT, to prepare Pr^{3+}-doped LT nanoparticles, the as-prepared Ta_2O_5 nanoparticles were mixed with a stochiometric amount of lithium hydroxide (LiOH) and 4.167 mol% of Praseodymium Oxide (Pr_2O_3).

$$Pr - doped\ LT \rightarrow LiTaO_3 + 4.167\ mol\%\ Pr_2O_3 \rightarrow LiTaO_3 - 4.167\ mol\%\ Pr \quad (29)$$

As for the Er^{+3}-Pr^{+3} co-doped configuration,

$$Pr-, Er - codoped\ LT \rightarrow LiTaO_3 + 4.167\ mol\%\ Pr_2O_3 + 4.167\ mol\%\ Er_2O_3 \quad (30)$$

All doping configurations were mixed in acetone with zirconia balls in a high-energy ball mill for 5 minutes. The resulting mixture was subsequently air-dried and then heat-treated in an oven at 650°C for 4 hours.

5.3 Results and Discussion

5.3.1 Pr^{3+}-doped and Pr^{3+}/Er^{3+}- co-doped LT powder characterization

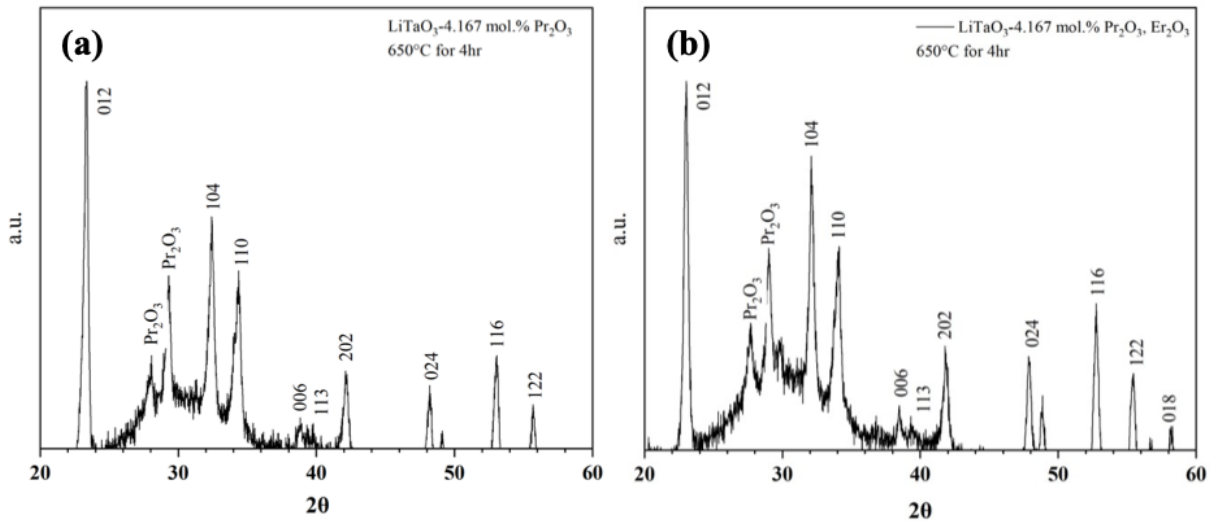

Figure 22: XRD analysis for (a) 4.167 mol% Pr^{3+}-doped and (b) 4.167 mol% Pr^{3+}-, Er^{3+}- co-doped LT nanoparticles.

Figure 22 (left) shows the XRD peaks of 4.167 mol% Pr^{3+}-doped LT nanoparticles. In this configuration, additional peaks corresponding to Pr_2O_3 emerge around $2\theta = 30°$, indicating the presence of excess Pr_2O_3. Similarly to the XRD analysis for Er^{3+}-doped LT, the incorporation of Pr^{3+} does not significantly modify the overall crystallographic structure of LT, regardless of whether Pr^{3+} occupies lithium or tantalum lattice sites. Higher-intensity peaks are present around $2\theta = 30°$ in the co-doped configuration, as both Pr_2O_3 and Er_2O_3 exhibit characteristic peaks, and their high intensities clearly demonstrate the nanocrystalline structure of Pr^{3+}-doped and Pr^{3+}/Er^{3+}-co-doped LT powders.

5.3.2 Pr^{3+}-doped and Pr^{3+}/Er^{3+}-co-doped LT Electronic bands and DOS

Figure 23 shows the electronic band structure with orbital projections, along with the corresponding total and orbital-projected DOS per orbital using the PBE functional. For all configurations, the valence band is dominated by the presence of O-p orbitals and the conduction band of Ta-pd orbitals. Hybridization between O-p and Ta-d orbitals indicates shared electronic states, signifying covalent bonding between Ta and O.

For Pr^{3+} replacing a Li site, the electronic bands show a band gap of 3.96 eV and the presence of Pr^{3+} 4f bands at the bottom of the conduction band. This is not the case for Pr^{3+} replacing a Ta site, as the bands are split above the Fermi level, yielding dual bandgaps of 1.29 eV and 1.65 eV. The intraband f–f transitions are favored when the 4f bands are partially occupied as the fragmented network will not allow complete transitions, which is not in the case for Pr^{3+} replacing a Ta site. For figure 21 (e–h), with 8.334% mol Er^{3+} configurations, similarly to 4.167% mol Er^{3+} configurations in figure 14(b & c), the Er^{3+} bands are present in the conduction band when Er^{3+} replaces Li and in the valence band when Er^{3+} replaces a Ta site. However, in contrast to the behavior observed for Er^{3+} substitution at the Li site, increasing the

Er^{3+} doping concentration does not reduce the bandgap, when Er^{3+} replaces Ta. This is attributed to the positioning of the Er^{3+} 4f states near the valence band maximum and the local structural distortions around the Er–O octahedra, which broaden the f-manifold without introducing significant band-tail states within the gap. In the Pr^{3+}/ Er^{3+}-co-doped configuration (with both ions occupying Li sites), hybridization occurs between the Er^{3+} 4f and Pr^{3+} 4f orbitals. This hybridization produces a broadened, more interactive f-manifold, resulting in significantly stronger intraband f–f optical transitions, as evidenced by the enhanced peaks in the imaginary part of the dielectric function. Consequently, the co-doped system exhibits improved optical properties compared with the singly doped cases.

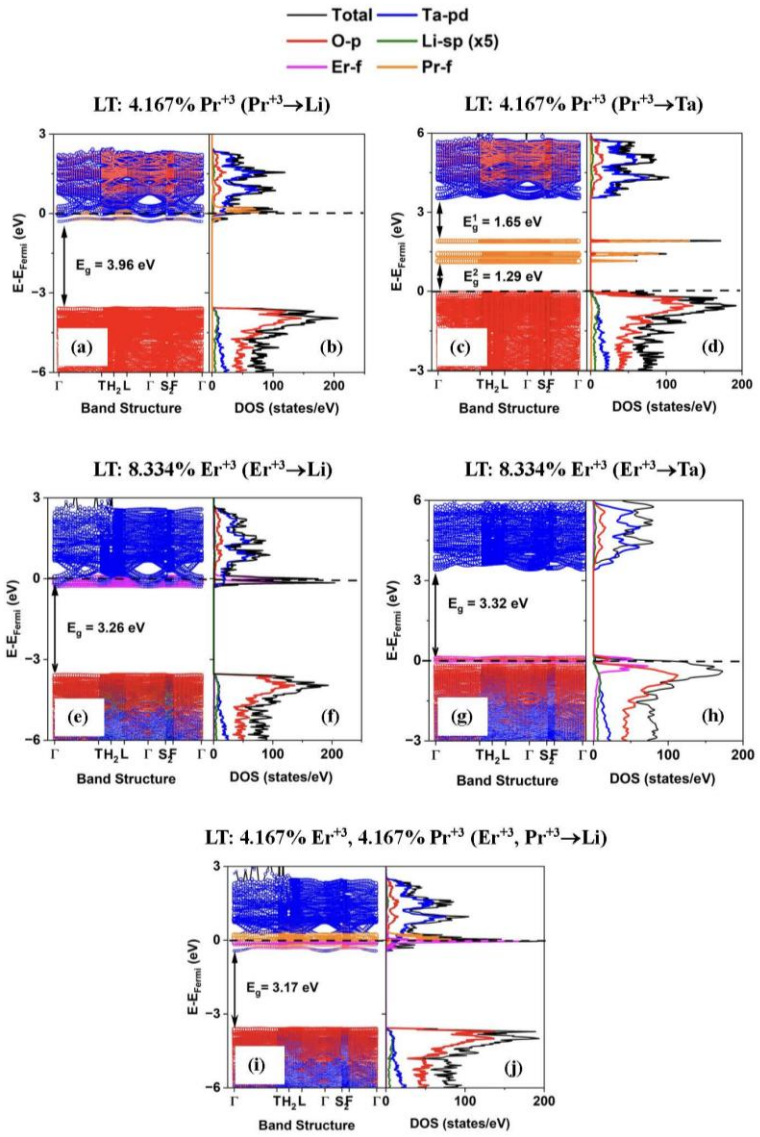

Figure 23. Electronic band structure with orbital projections (a, c, e, g, and i) and corresponding total and projected DOS per orbital (b, d, f, h, and j) using the PBE calculations for the following LT doped configurations (a) and (b) LT: 4.167% Pr^{3+} with Pr^{3+} at the Li site (Pr^{3+}→ Li), (c) and (d) LT: 4.167% Pr^{3+} with Pr^{3+} at the Ta site (Pr^{3+}→ Ta), (e) and (f) LT: 8.334% Er^{3+} with Er^{3+}at the Li site (Er^{3+}→ Li), (g) and (h) LT: 8.334% Er^{3+} with Er^{3+}at the Ta site (Er^{3+}→ Ta), and (i) and (j) LT: 4.167% Er^{3+}, 4.167% $Pr^{3+}$with $Pr^{3+}$and Er^{3+}at the Li site (Er^{3+}, Pr^{3+}→ Li). Note. Reprinted from [171]. In this dissertation, the ion notation is written as X^{3+} to be consistent with standard chemical notation, whereas the original published figure used X^{+3}.

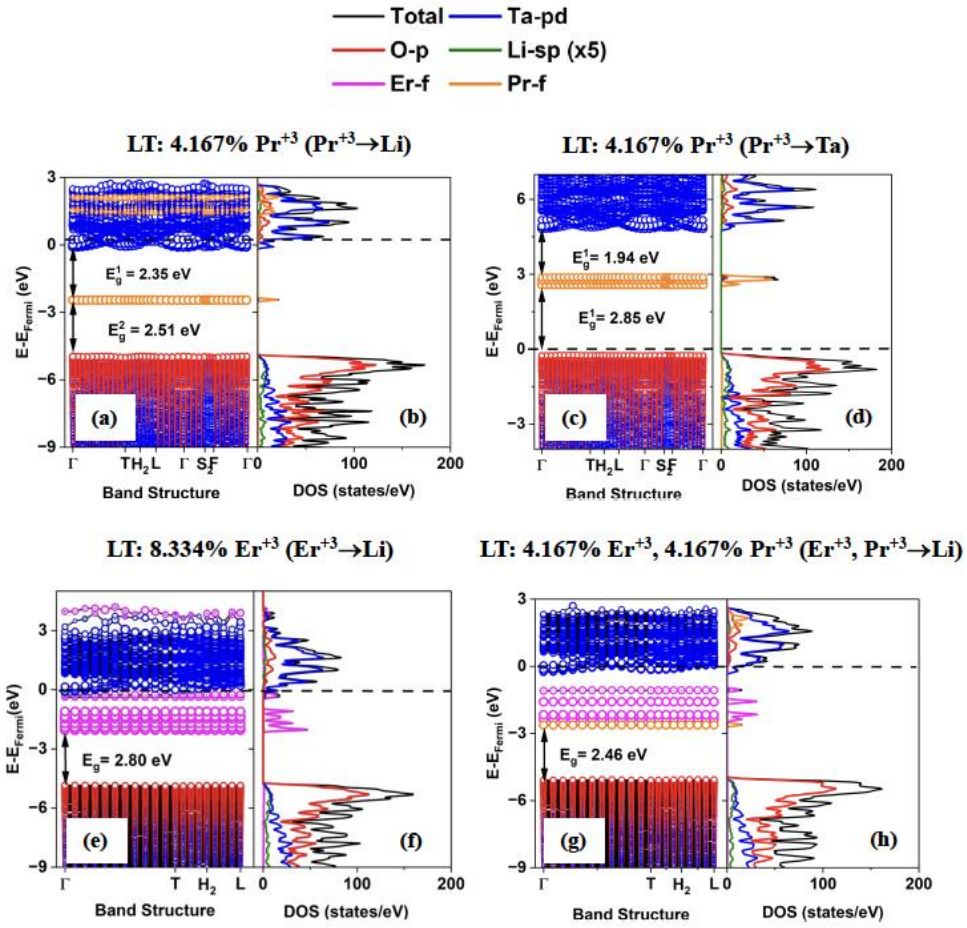

Figure 24: Electronic band structure with orbital projections (a, c, e, g, and i) and corresponding total and projected DOS per orbital (b, d, f, h, and j) using the HSE06 calculations for the following LT doped configurations (a) and (b) LT: 4.167% Pr^{3+} with Pr^{3+} at the Li site (Pr^{3+} → Li), (c) and (d) LT: 4.167% Pr^{3+} with Pr^{3+} at the Ta site (Pr^{3+} → Ta), (e) and (f) LT: 8.334% Er^{3+} with Er^{3+} at the Li site (Er^{3+} → Li), (g) and (h) LT: 4.167% Er^{3+}, 4.167% Pr^{3+} with Pr^{3+} and Er^{3+} at the Li site (Er^{3+} → Ta). Note. Reprinted from [171]. In this dissertation, the ion notation is written as X^{3+} to be consistent with standard chemical notation, whereas the original published figure used X^{+3}.

Figure 24 presents the HSE06 calculations for all configurations but 8.334% mol Er^{3+} case, in which Er^{3+} replaces a Ta site, as the electronic information is computationally too expensive to obtain. As expected, the HSE06 functional yields larger band gaps compared to

standard DFT functionals. In the case of Pr^{3+} configurations, the splitting of the Pr^{3+}-4f levels induces a subdivided energy gap structure. This behavior contrasts with the Er^{3+}-doped configurations, where the Er^{3+} 4f states remain more localized and are positioned below the conduction band. Although HSE06 calculations are more computationally demanding, they provide more reliable band gaps and a better description of the positions of the lanthanide 4f orbitals.

5.3.3 Optical properties of Pr^{3+}-doped and Pr^{3+}/Er^{3+}co-doped LT.

Figure 25 shows the optical properties for all the LT configurations presented. For the imaginary part of the dielectric function, ε_I, energies within 0.0–0.5 eV correspond to Er^{3+} and Pr^{3+} intraband f–f transitions. The absorption intensities in this region decrease in the following order: Pr^{3+}/Er^{3+}-co-doped LT > 4.167% mol Pr^{3+}-doped LT at a Li site >8.334% mol. Er^{3+}-doped LT at Ta site > 8.334% mol. Er^{3+}-doped LT at Li site > 4.167% mol. Er^{3+}-doped LT at Li site >4.167% mol. Er^{3+}-doped LT at Ta site. Pr^{3+}-doped configurations exhibit stronger absorption intensities than Er^{3+}-doped configurations, which is attributed to the higher number of vacancies present in the Pr^{3+} structures.

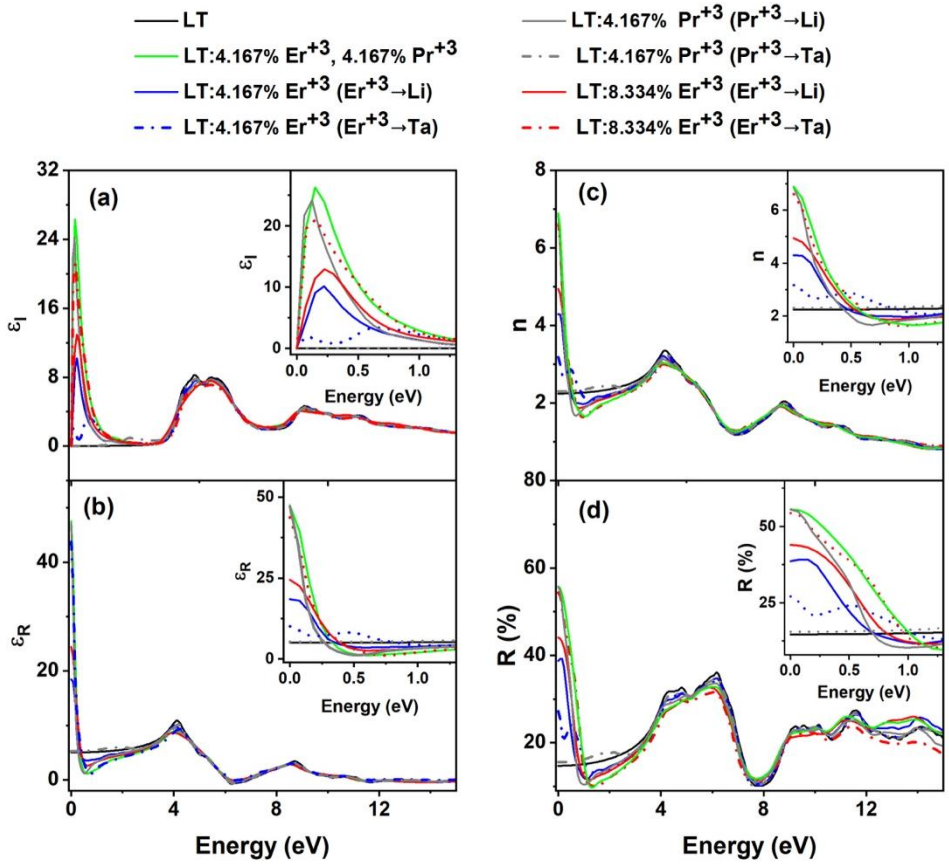

Figure 25. a) The frequency-dependent imaginary part of dielectric functions ε_I for LT and its Er^{3+} and Pr^{3+} doped and co-doped counterparts for Er^{3+} and Pr^{3+} at the Li site (Er^{3+}, Pr^{3+} → Li) and the Ta site (Er^{3+}, Pr^{3+} → Ta), b) the real part ε_R, c) the refractive index n, and d) the reflectivity R. Note. Reprinted from [171]. In this dissertation, the ion notation is written as X^{3+} to be consistent with standard chemical notation, whereas the original published figure used X^{+3}.

The dielectric constant, $\varepsilon_R(0)$, static refractive index, $n(0)$, and the static reflectivity $R(0)$ show a similar trend to ε_I. These variations in the dielectric constant indicate that both the co-doped configuration and the LT:4.167% Pr^{3+} (Pr^{3+}→Ta) are better dielectrics than all other doped configurations here. Due to high absorption coefficients in ε_I, high refractive indices are foreseen and proven. Specifically, the static refractive indexes are correlated with f–f intraband transitions; a higher $n(0)$ value indicates a narrower energy gap between the two 4f bands. Furthermore, variations in the static reflectivity $R(0)$, demonstrate that doping and co-doping

alter the optical behavior of a material. Notably, LT:4.167% Pr^{3+} (Pr^{3+}→Li) has a high $R(0)$ value, which speaks of the mirror nature in the IR range.

5.3.4 QTAIM and ELF analysis of Pr^{3+}-doped and Pr^{3+}/Er^{3+}-co-doped LT.

As previously mentioned, QTAIM uses topological analysis of the gradient paths to define chemical bonds, predict their multiplicities, and determine atomic boundaries within molecules. Table 1 shows the calculated QTAIM properties for the metal-O bond critical points for pure and all doping configurations of LT.

Table 1: QTAIM parameters at the Li–O, Ta–O, and X–O for X = Er^{3+}, Pr^{3+} bond critical points (3, -1) and their corresponding interatomic distances for LT, LT:4.167% Er^{3+} and LT:8.334% Er^{3+} with Er^{3+} located in the Li or the Ta site, and the LT: 4.167% $Pr^{3+}$and LT: 4.167% Er^{3+}, 4.167% Pr^{3+}, with the dopant atoms in the Li site. Only the QTAIM properties, which correspond to the smaller metal-bond critical point-oxygen distances, are shown for the doped configurations. Note. Reprinted from [171]. In this dissertation, the ion notation is written as X^{3+} to be consistent with standard chemical notation, whereas the original published table used X^{+3}.

Configuration	Distances	QTAIM properties			
	(Å)	(a.u.)			
	Li–O (Ta–O) [X–O], X = Er^{3+}, Pr^{3+}	$\rho(\vec{r}_b)$	$\nabla^2\rho(\vec{r}_b)$	$(H/\rho)(\vec{r}_b)$	$(\lvert V\rvert/G)(\vec{r}_b)$
LT	2.021	0.024	0.162	0.315	0.787
	2.312	0.012	0.076	0.370	0.690
	(1.929)	(0.154)	(0.557)	(-0.518)	(1.361)
	(2.066)	(0.109)	(0.403)	(-0.345)	(1.271)
LT:4.167% Er^{3+} (Er^{3+}→ Li)	2.001	0.025	0.200	0.415	0.736
	(1.927)	(0.155)	(0.453)	(-0.583)	(1.443)
	[2.207]	[0.076]	[0.300]	[-0.189]	[1.162]
LT: 4.167% Er^{3+} (Er^{3+}→ Ta)	1.968	0.028	0.174	0.252	0.807
	(1.925)	(0.156)	(0.484)	(-0.573)	(1.426)
	[2.165]	[0.085]	[0.300]	[-0.259]	[1.227]
LT:8.334% Er^{3+} (Er^{3+}→ Li)	2.009	0.025	0.060	-0.050	1.078
	(1.932)	(0.151)	(0.573)	(-0.498)	(1.344)
	[2.156]	[0.086]	[0.339]	[-0.227]	[1.187]
LT:8.334% Er^{3+} (Er^{3+}→ Ta)	1.907	0.032	0.037	-0.196	1.408
	(1.880)	(0.174)	(0.618)	(-0.601)	(1.404)
	[2.150]	[0.088]	[0.307]	[-0.275]	[1.239]

(Table 1 cont.)

LT: 4.167% Pr^{3+} (Pr^{3+}→ Li)	1.996	0.027	0.164	0.284	0.801
	(1.853)	(0.156)	(0.582)	(-0.527)	(1.353)
	[2.230]	[0.088]	[0.283]	[-0.306]	[1.278]
LT: 4.167% Er^{3+}, 4.167% Pr^{3+} (Er^{3+}, Pr^{3+}→ Li)	1.991	0.027	0.026	-0.176	1.420
	(1.936)	(0.151)	(0.549)	(-0.501)	(1.358)
Er^{3+}– O	[2.225]	[0.073]	[0.306]	[-0.151]	[1.123]
Pr^{3+}–O	[2.243]	[0.086]	[0.270]	[-0.296]	[1.274]

The first column denotes the atomic distances per metal-O bond, the second the electron density ($\rho(\vec{r_b})$, the Laplacian electron density ($\nabla^2\rho(\vec{r_b})$, indicates whether the electron density is locally present), the total electron energy density ratio on the fourth column, and lastly, the Virial ratio presented in chapter 3. For all configurations, $|V_b|/G_b < 2$, and $\nabla^2\rho_b(\vec{r}) > 0$, which indicates the interaction between two atoms is of a shared shell. Moreover, the Li–O electron density and its Laplacian at the Li–O bond critical point are smaller than their Ta–O counterparts, indicating weaker Li–O bonding. In agreement with the DOS presented in figure 14, where the small overlap between Li and O orbitals, compared to the stronger Ta–O hybridization, suggests that Li–O bonds are weaker than Ta–O bonds. Although the electronic bands suggested strong covalent Ta–O bonding, the Ta–O is an incipient covalent ($1< |V_b|/G_b < 2, H_b < 0$) for all configurations within the QTAIM analysis.

For the LT:8.334% Er^{3+}-doped and the co-doped Pr^{3+}/Er^{3+}configuration, the shortest Li–O interaction appears incipient covalent due to the increased coupling between these two atoms' sp orbitals, whereas longer Li–O distances correspond to closed shell interactions along the valence in the electronic bands from figure 21. Furthermore, Er^{3+}–O and Pr^{3+}–O exhibit incipient covalent bonding, with the Pr^{3+}–O distance larger than the Er^{3+}–O distance ($1< |V_b|/G_b < 2, H_b < 0$).

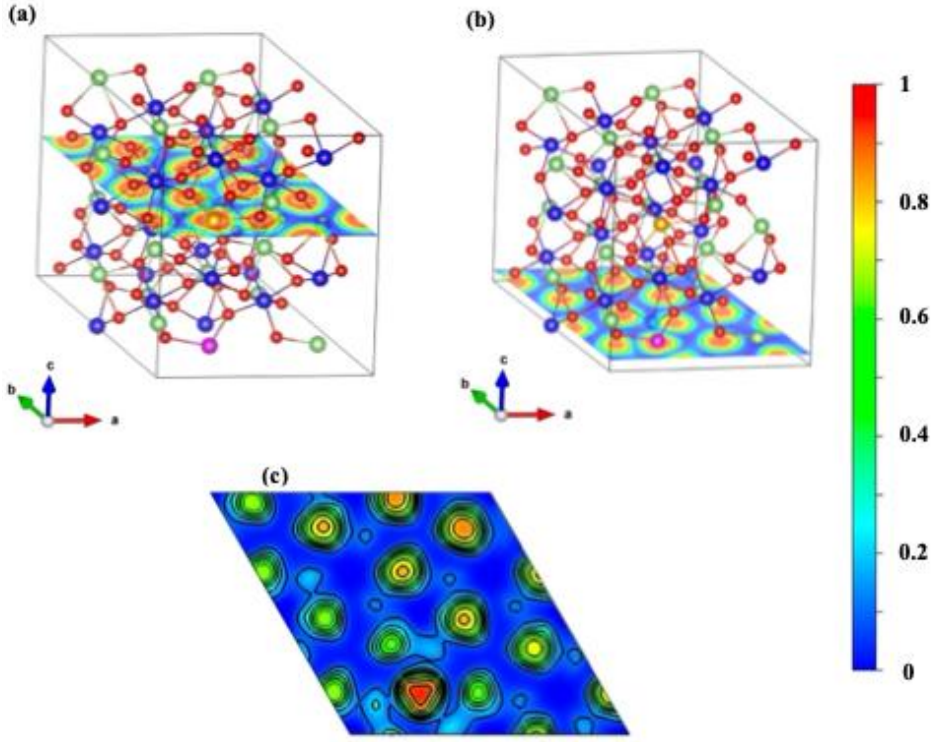

Figure 26: ELF contour maps for the LT: 4.167% Er^{3+}, 4.167% Pr^{3+} unit cell (a) at the plane (001) passing through the Er^{3+} atom and (b) the Pr^{3+}atom. (c) ELF at the plane defined by $Pr^{3+}$and the new nearest O atoms. Red, strong localization (ELF =1); Green free electron gas (ELF = 1/2); Blue, no localization (ELF = 0). Note. Reprinted from [171].

Figure 26 shows the ELF contour maps for the LT: 4.167% Er^{3+}, 4.167% Pr^{3+} unit cell at various planes. Because the ELF maps for the other configurations are similar, they are not reported here. The localized electron density is concentrated around the Ta, Er^{3+}, and Pr^{3+} atoms, whereas no significant ELF is observed around Li. The ELF values approach zero in the regions between the metal cations and oxygen anions, indicating the absence of strong covalent bonding between these atoms. Moreover, the ELF around the Ta, Er^{3+}, and Pr^{3+} atoms is distorted due to limited orbital overlap, consistent with our QTAIM findings.

5.3.5 Pr^{3+}-doped and Pr^{3+}/Er^{3+}-co-doped LT photoluminescence analysis

As shown in Figure 27, both LT configurations exhibit their strongest visible emissions at 600–650 nm. For LT: 4.167 mol% Pr_2O_3 configuration, the configuration also exhibits strong infrared emission at 1100–1140 nm. In contrast, the co-doped LT: 4.167 mol% Pr_2O_3, 4.167 mol% of Er_2O_3 configuration displays weak emissions 400–550 nm within the visible range alongside stronger emissions for 1050–1130 nm, 1150–1250 nm in the infrared region.

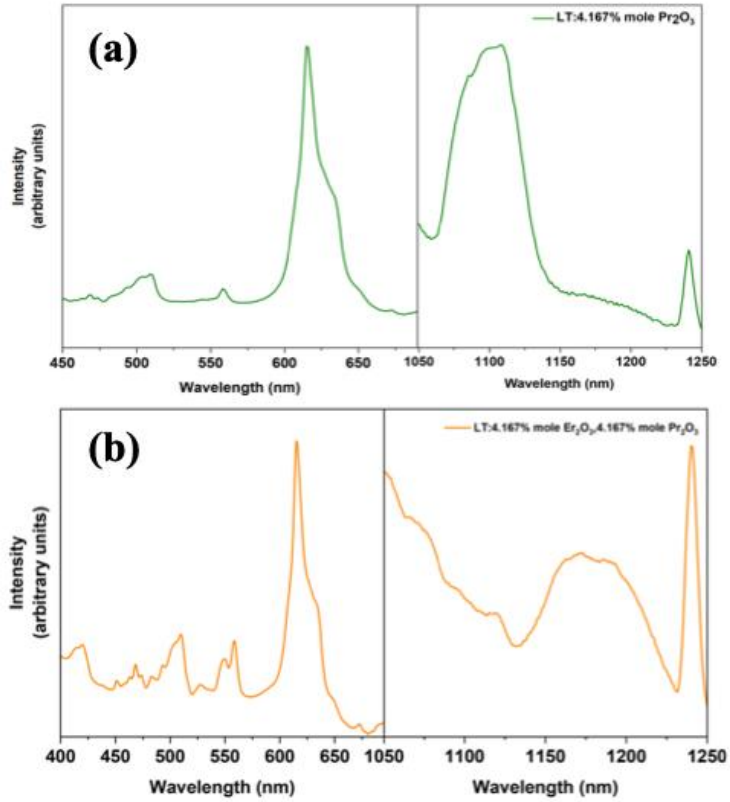

Figure 27: The fluorescence emission spectra for (a) LT: 4.167 mol% of Pr_2O_3 and (b) co-doped LT: 4.167 mol% Pr_2O_3, 4.167 mol% of Er_2O_3 in the visible region and the near IR.

CHAPTER VI

BORON-NITRIDE SILVER (Ag/defect *h*-BN) NANOCOMPOSITE

6.1 Calculation Parameters

6.1.1 Supercell modeling

Figure 28 (a) and (b) shows the DFT-optimized pristine *h*-BN 4×4×1 supercell with 16 B and 16 N atoms (32 atoms in total). Each boron atom is coordinated with three nitrogen atoms in a hexagonal lattice. In the Ag-decorated *h*-BN (Ag/*h*-BN) supercell, the Ag atom sits atop the vacancy (at either the B or N site).

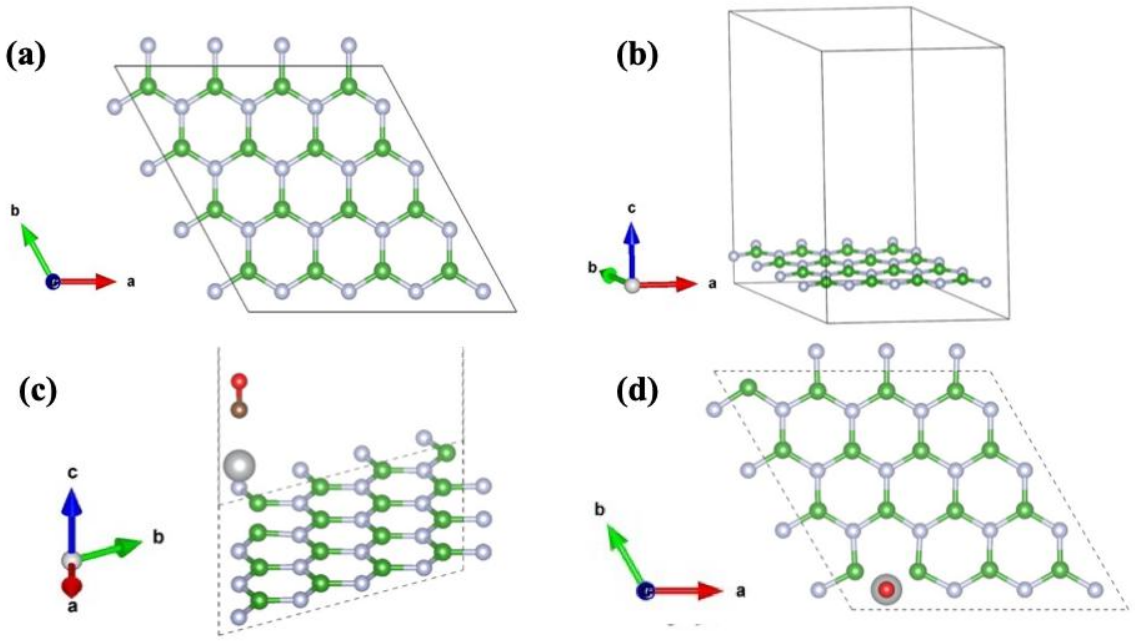

Figure 28. (a)Top view of the DFT h-BN monolayer, (b) its side view, (c) Side view of the optimized defect h-BN monolayer with Ag atop of N defect with the absorbed CO. (d) its top view. Atoms are colored as follows: B, green; N, gray; C, brown; O, red; Ag, gray.

6.1.2 Parameters for *h*-BN-related calculations

Electronic structure calculations, optimal geometries, and the dielectric functions were obtained for the pristine *h*-BN, defect *h*-BN (vacancy on B or N site), double vacancy *h*-BN (adjacent vacancies on B and N sites), Ag decorated *h*-BN defect sites, and Ag decorated *h*-BN defect sites with and without CO. GW Approximation calculations were performed using quasiparticle energies by improving upon DFT electronic structure results. Maximally localized Wannier functions were subsequently generated using WannierTools for band interpolation. Furthermore, BSE calculations were performed to accurately describe neutral excitations and optical response across all *h*-BN configurations.

The kinetic energy cutoff for all calculations is 550 eV, which ensures the integrity of our results. The energy convergence criteria were set at 10^{-9} eV, and the geometry optimization criteria at 10^{-4} eV/Å per atom. The Brillouin zone was sampled using the Γ-centered 6×6×1 grid.

6.2 Sample Preparation

6.2.1 Ag/ *h*-BN preparation

The following synthetic route is mentioned in Ref.[172]. Boron nitride and silver nitrate were introduced into a 50 mL Teflon-lined stainless-steel autoclave containing 30 mL of N, N-dimethylformamide (DMF). Subsequently, 0.1 mmol of polyvinylpyrrolidone (PVP) was added to the solution. The autoclave was sealed and maintained at 160°C for 8 hours. After the reaction, the autoclave was allowed to cool to room temperature. The resulting product was collected and washed three times with deionized water and ethanol. Finally, the washed product was dried at 80°C for 12 hours to obtain the final material. The synthetic route yielded an Ag sample with an 80% metal weight. Subsequently, a second sample with 30% Ag by weight was synthesized using the same method for comparative analysis, aiming to evaluate the impact

of silver content on the conductivity of *h*-BN and to determine the optimal composition for gas sensing applications.

The synthesized material is denoted Ag/*h*-BN. Incorporation of Ag during synthesis may introduce lattice perturbations and defect sites in *h*-BN [126, 173, 174]. However, the presence and concentration of such defects were not experimentally verified in this work.

6.2.2 Ag/*h*-BN pellet preparation

To fabricate the gas-sensing ceramic pellet, the synthesized Ag/*h*-BN powder was loaded into a cylindrical steel die and dry-pressed. A punch was placed above the powder, and the die assembly was inserted into a manual hydraulic press. A compressive force of up to 8 tons was applied and held for 1 minute, forming a solid pellet suitable for gas-sensing measurements. The resulting pellet had a diameter of 10 mm and a thickness of 1.52 mm.

6.3 Results and Discussion

6.3.1 Ag/defect *h*-BN Electronic bands and Density of States (DOS)

Figure 29 presents the calculated electronic band structure and density of states (DOS) for both pristine and defect *h*-BN monolayers. For all configurations, the valence band top is dominated by N-sp orbitals, whereas the conduction band bottom is primarily composed of B-sp orbitals.

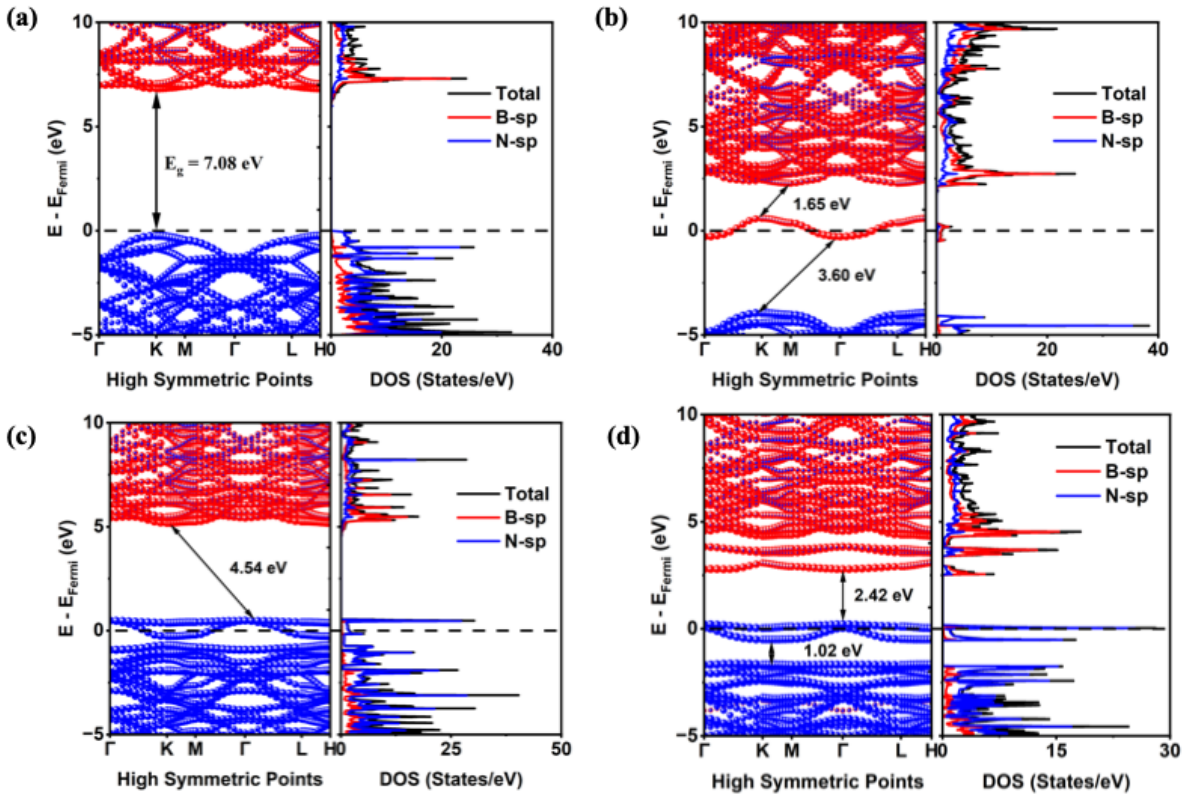

Figure 29: Wannier interpolated G_0W_0 calculations for the electronic band structure with orbital projections and the corresponding total and projected DOS per orbital from the G_0W_0 calculations for (a) pristine h-BN, (b) defect h-BN on N site, (c) defect h-BN on B site, and (d) defect h-BN on B and N sites.

For pristine *h*-BN, the calculated bandgap is 7.08 eV. This value agrees with reports in the literature, where measured *h*-BN bandgap energies widely range from 3.6 to 7.1 eV [175]. Because *h*-BN possesses a bandgap significantly larger than 2 eV, it is considered an insulating material [176]. The DOS of pristine *h*-BN illustrates a clear hybridization of B and N orbitals. Specifically, N atom contributions dominate the top of the valence band, whereas the overlap at the bottom of the conduction band is minimal, with B atom contributions being dominant.

Figure 29 (b)–(d) shows the calculated band structures for point-defective *h*-BN at isolated and adjacent sites. It is evident that the introduction of vacancies significantly alters the

electronic bands of *h*-BN. For defect *h*-BN with an N vacancy, new states near the Fermi level appear, leading to the reduction in the band gap. These new states near the Fermi level arise from the breaking of the bond between B and N, thus leaving two unbonded B atoms. Furthermore, a dual-band gap is observed between the Fermi level and the bottom of the conduction band, with a magnitude of 1.65 eV, alongside a 3.60 eV bandgap extending from the Fermi level to the top of the valence band. As for the defect *h*-BN with a B vacancy, the bandgap decreases from 7.08 eV to 4.54 eV. The B vacancy introduces a new level but remains localized near the top of the valence band, leaving three N atoms unbonded due to its hexagonal nature. Lastly, adjacent B and N vacancies exhibit a dual-band gap between the Fermi and the bottom of the conduction band with a magnitude of 2.42 eV alongside a 1.02 eV bandgap extending from the Fermi to the top of the valence band. Even though the introduction of vacancies reduces the bandgap by creating new states, this does not imply the material is more conductive, as the fragmented network will not allow complete transitions.

Figure 30 presents a comparative analysis of the calculated electronic band structures and corresponding density of states (DOS) for Ag-decorated defect *h*-BN, both isolated and in the presence of CO. This comparison highlights the electronic modifications induced by the gas.

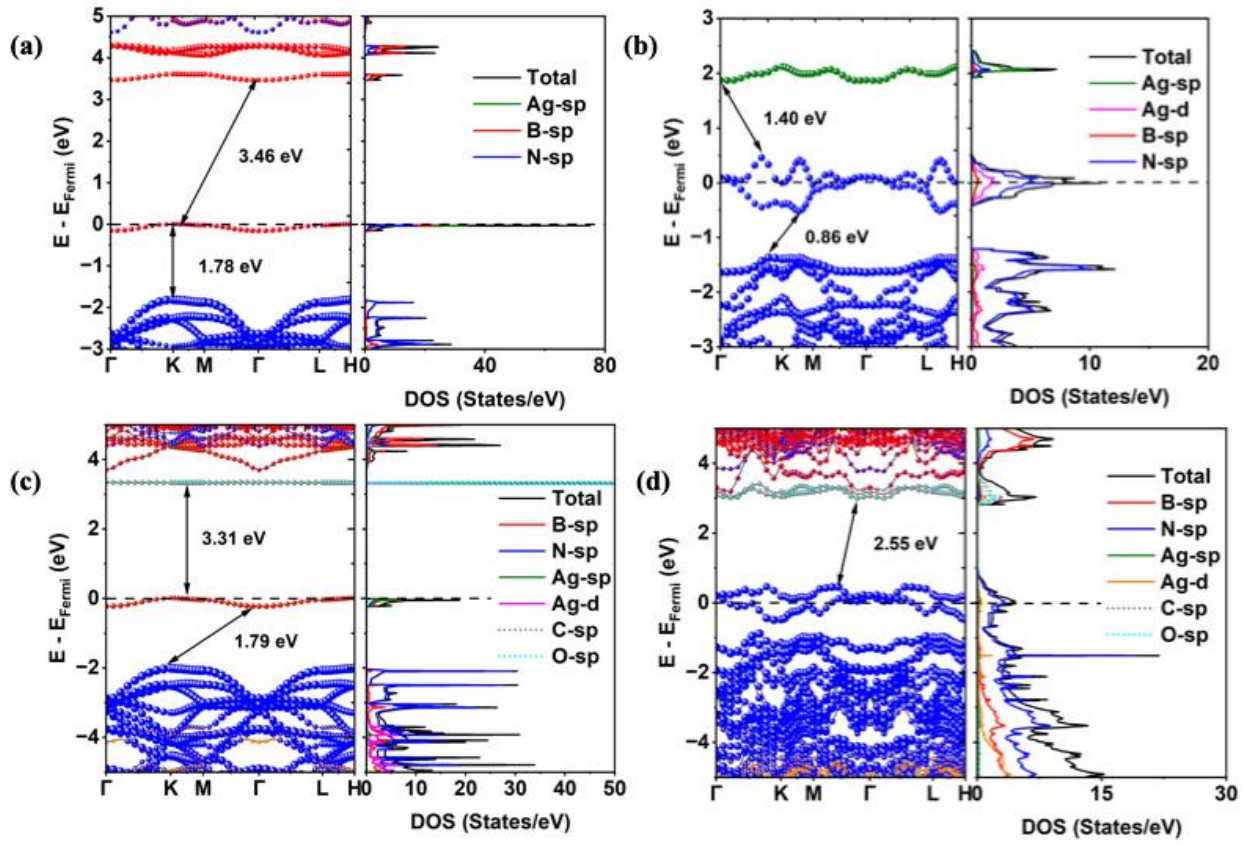

Figure 30: Wannier interpolated G_0W_0 calculations for the electronic band structure with orbital projections and the corresponding total and projected DOS per orbital from the G_0W_0 calculations for (a) Ag decorated h-BN defect at N site, (b) Ag decorated h-BN defect at B site, (c) Ag decorated h-BN defect at N site with CO, and (d) Ag decorated h-BN defect at B site with CO.

Similarly to the defect *h*-BN at the N site, Ag decorated *h*-BN defect at the N site exhibits a dual-band gap of 3.46 eV gap that separates the mid-gap states from the bottom of the conduction band, while a 1.78 eV gap extends from the Fermi level to the top of the valence band. New states within the Fermi level emerge from the breaking of the bond between B and N, thus leaving two unbonded B atoms, as demonstrated in Figure 28(c). Following Ag decoration, the DOS reveals a localized hybridization between the Ag-sp and B-sp orbitals. This localization implies a weak electronic interaction between the B and N atoms, suggesting that introducing vacancies at an N site is not energetically favorable. Rather than a simple narrowing of the

bandgap, this electronic reconfiguration yields new absorption energies, which arise directly from the orbital hybridization within these newly emerged localized states, as shown from the DOS.

Upon exposure to CO, Figure 30(c) shows minimal orbital hybridization near the Fermi level and the emergence of large dual-band gaps measuring 3.31 eV and 1.79 eV. Furthermore, the CO molecule only weakly perturbs the system; its electronic states remain highly localized around 3.3 eV, indicating a weak interaction with the Ag-decorated defect *h*-BN at the N site lattice. In the case of the Ag-decorated *h*-BN with a B-site defect, this configuration is optimal for gas-sensing applications when in contact with CO: (1) the strong orbital hybridization in the conduction band suggests strong biding energy, and (2) the strategic implementation of lattice defects evidently enhances the optoelectronic properties of the host material by reducing the bandgap to 2.55 eV.

6.3.2 Adsorption energy and band-structure connection

The adsorption-energy results show that CO interacts very differently with the two Ag-decorated vacancy sites in *h*-BN. For Ag@V_N, the CO adsorption energy is approximately 0 eV, indicating a very weak or physisorption-like interaction. This agrees with the electronic structure: the system maintains a relatively large band gap of about 3.31 eV, Ag remains essentially closed shell d^{10}, and there is minimal hybridization near the Fermi level.

In contrast, for Ag@V_B, CO adsorption is much stronger, with an adsorption energy of about −1.0 eV. This stronger binding is reflected directly in the band structure by a reduced gap of about 2.55 eV and the appearance/shift of defect-derived states closer to the Fermi level. Therefore, the stronger adsorption at the B-vacancy site is not simply due to Ag d-state donation,

but is mainly defect-controlled, with Ag acting as a structural mediator that enables stronger CO–defect interaction.

6.3.3 Optical properties of Ag/*h*-BN

As previously stated, the experimentally measurable quantities, imaginary part of the dielectric function (ε_I), can be used to determine the dispersion of a material. For pristine *h*-BN, in the first panel of Figure 31, strong peaks are present in the 5–6 eV range, indicating absorption in the UV range. The introduction of point defects creates defect-induced states near the Fermi level. Consequently, new absorption peaks emerge near the Fermi level for defect-engineered *h*-BN at both the N and B sites, as well as a distinct low-energy peak near 0.3 eV for defect *h*-BN at the B site.

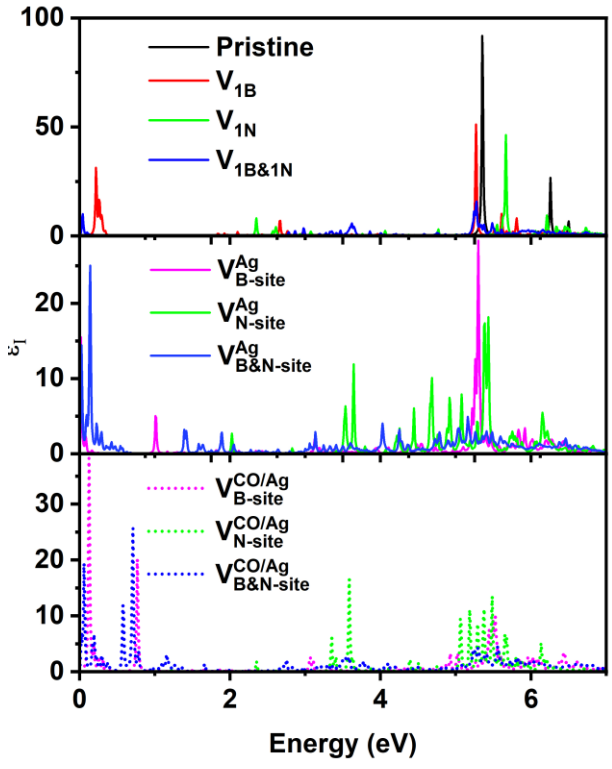

Figure 31:The imaginary part of the dielectric function for all configurations of h-BN with and without the presence of CO.

For Ag-decorated defect *h*-BN (second panel), stronger absorption peaks are present in the UV range upon the incorporation of vacancies at B and N sites. Furthermore, the emergence of new absorption peaks for the B-site defect and the combined B- and N-site defects denotes hybridization between the Ag and *h*-BN lattices. This hybridization is important as it demonstrates a strong interaction between the BN substrate and Ag. Lastly, when exposed to CO, the interaction between Ag and C atoms further modifies ε_I at absorption energies along the Fermi level. Defect *h*-BN at the B site shows higher absorption peaks than any other configuration, indicating a superior optical sensitivity and stronger binding to the C atom. Although point defects cannot be completely isolated or controlled experimentally, the calculations presented serve as proof that the introduction of specific lattice defects and noble metals, such as Ag, successfully enhance the electro-optical properties of *h*-BN for gas-sensing applications.

6.3.4 Ag/*h*-BN powder characterization

One of the primary objectives is to obtain Ag/*h*-BN nanocomposite; accordingly, XRD and SEM analyses were conducted to study the morphology and crystallographic structure of the prepared material.

Figure 32 (a) and (b) illustrate the XRD patterns and corresponding crystallographic structures for pristine *h*-BN and silver nitrate ($AgNO_3$) precursors. Both samples exhibit amorphous humps alongside high-intensity counts, indicating the presence of nanoparticles. Precursors have characterization peaks present at 17°, 26°, 41°, 54°, and 75° for BN and 30°, 40°, 48°, and 69° within the 2θ range for $AgNO_3$. Figure 32(c) presents the XRD profiles of the as-prepared Ag/defect *h*-BN nanocomposite at 30-wt.% and 80-wt.% of Ag; both compositions showcase a dominant presence of Ag and a high count, reinstating the presence of nanosized

particles. Notably, the characteristic peaks of the BN matrix are more prevalent in the 30-wt.% Ag configurations in comparison to the 80-wt.% Ag.

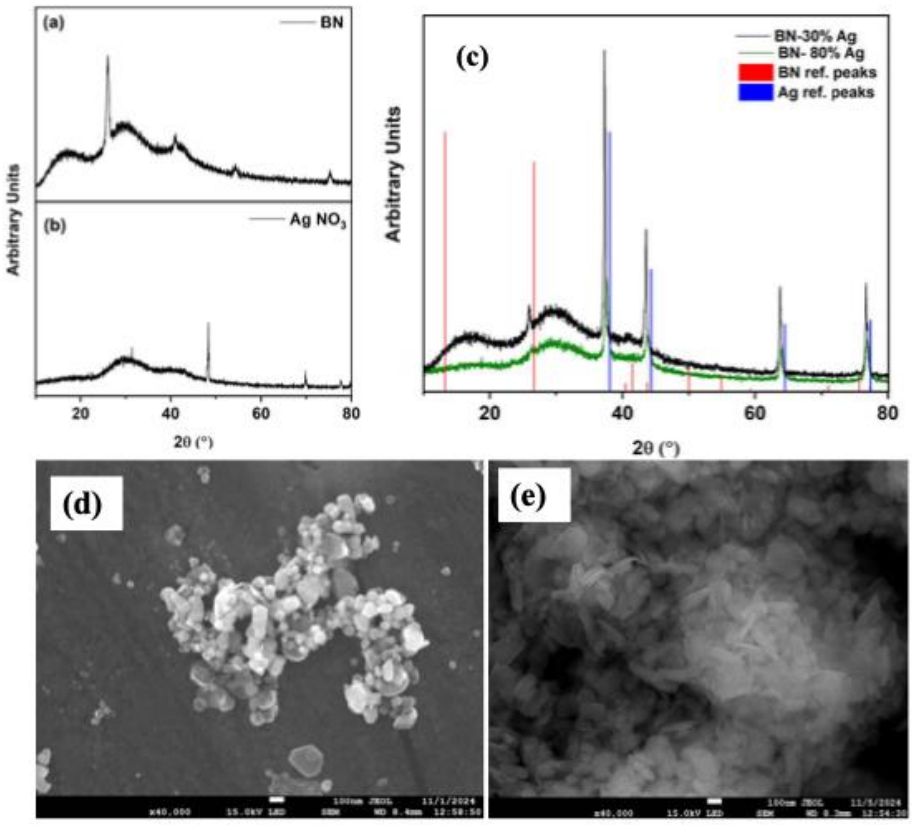

Figure 32: XRD analysis for (a) h-BN precursor, (b) AgNO3 precursor, and (c) different configurations of Ag/h-BN nanocomposite; SEM analysis of (d) h-BN-80wt.% Ag powder & (e) h-BN precursor.

Figure 32 also displays the SEM analysis for (d) *h*-BN-80wt.% Ag nanocomposite and (e) BN precursor. The BN precursor observed at 40,000x magnification (scale bar = 100nm) exhibits a homogeneous, flat, disk-shaped nanoparticle morphology with a smooth surface. This uniform structure indicates a good particle dispersion and provides a large specific surface area, making BN an ideal substrate for future surface modifications. As-prepared Ag/*h*-BN powder, observed

at 40,000x magnification, displays a consistent distribution of silver nanoparticles that appear as brighter regions due to their conductivity. The silver forms a homogeneous layer across the *h*-BN surface, resulting in a consistent particle size distribution.

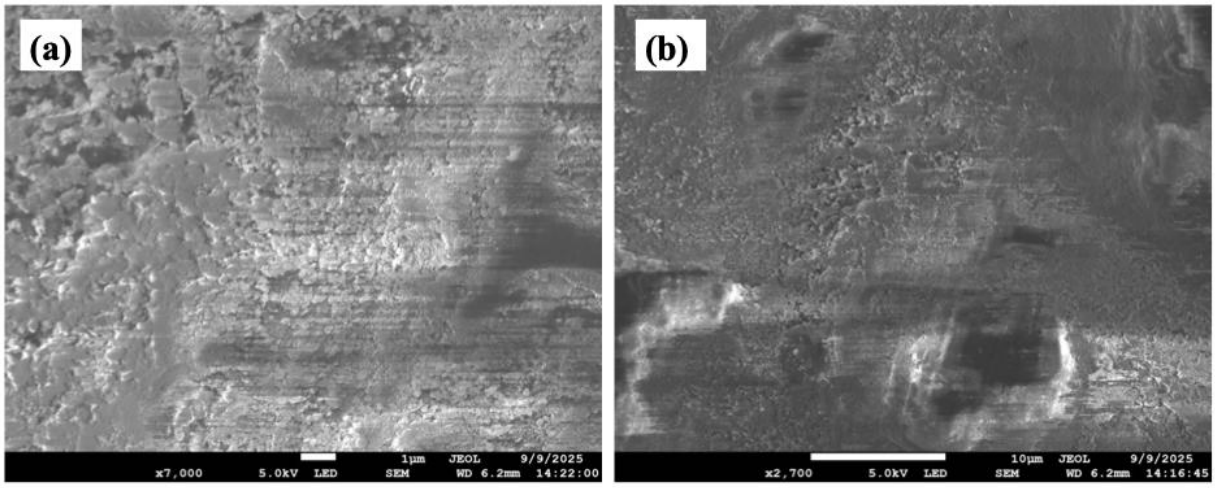

Figure 33: SEM analysis h-BN-30wt.% Ag pellet sintered pellet at (a) 1µm and (b) 10 µm scale

Figure 33 revealed smooth surfaces and tightly bonded grains with minimal porosity across different magnifications, indicating a well-sintered pellet. Furthermore, SEM analysis shows varying degrees of neck formation among particles; however, this is too small a scale to raise concerns about the contact between the 4-point probe machine and the sample. Cracks are not visible within the sample, suggesting no thermal stress was present.

6.3.5 DSC/TGA analysis

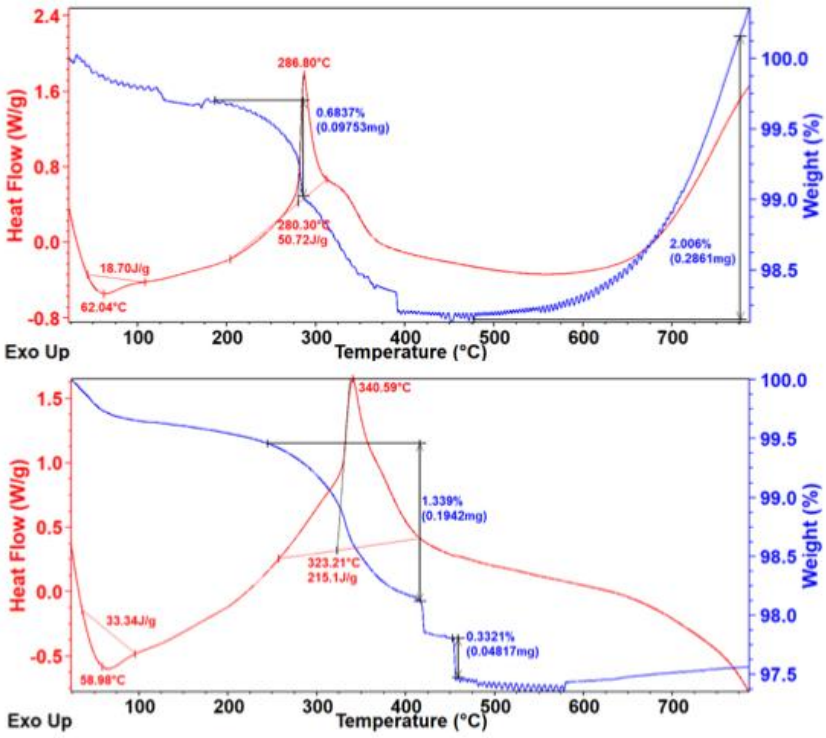

Figure 34:DSC/TGA analysis of h-BN-80wt.% Ag powder in (top) air and in (bottom) argon.

The oxidation behavior of the *h*-BN-80wt.% Ag powder in air was evaluated using thermogravimetric analysis (TGA). As shown in Figure 34(a), the TGA analysis reveals an initial exothermic reaction of 50.72 J/g at 280°C, corresponding to a weight loss of 0.6837%. This slight initial mass reduction is likely attributed to the evaporation of trapped solvents and early-stage thermal decomposition. Notably, oxidation of the Ag/*h*-BN powder begins at a relatively high temperature of 500°C, as evidenced by a 2% weight gain as the temperature increases. Conversely, in an argon atmosphere, the Ag/*h*-BN powder shows no oxidation, underscoring the critical importance of sintering in a noble-gas environment.

6.3.6 Conductivity testing of Ag/*h*-BN with CO exposure.

All resistance measurements were performed in a laboratory setting at room temperature, 50%–52% relative humidity, and under a 1000 ppm CO gas flow. The flow rate was maintained at 100 mL/min using a calibrated flowmeter.

Figures 35 and 36 illustrate variations in electrical resistance that indicate chemically resistive reactions in the Ag/*h*-BN pellets during gas exposure. Measurements were conducted using a four-point probe system. Each test began with a 60-second baseline reading in the absence of gas, followed by a 60-second gas-exposure phase. The duration of subsequent cyclic readings varied with the specific recovery response of each specimen.

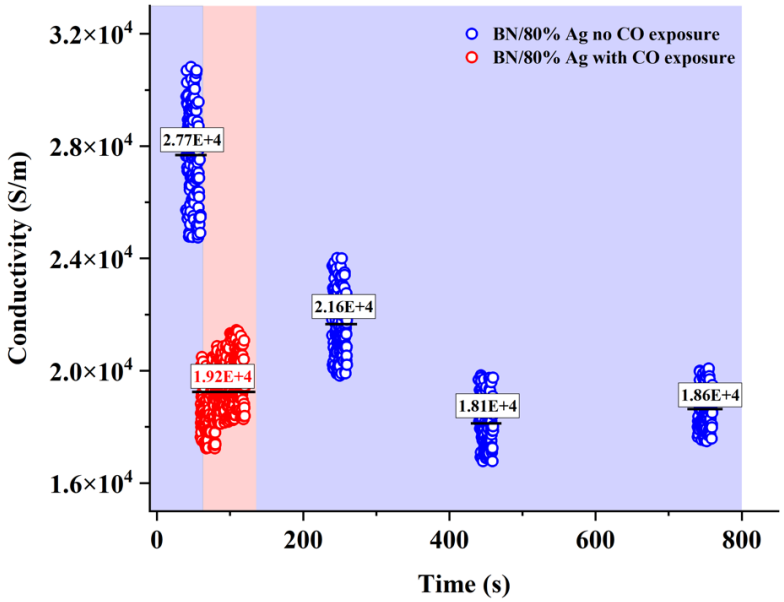

Figure 35: Conductivity results for h-BN-80wt.% Ag pellet under CO exposure.

For the *h*-BN-80wt.% Ag pellet, shows a high-baseline conductivity of $2.77*10^4$ S/m with an immediate 30% decrease to 1.92×10^4 S/m when exposed to CO. Subsequent exposure cycles are omitted from Figure 35 because the pellet failed to recover. This lack of recovery is

attributed to complete saturation, which prevents the natural desorption of CO molecules from the Ag atoms. Thermal activation may be required for cyclic testing of the Ag to release the bound CO molecules and recover its baseline conductivity.

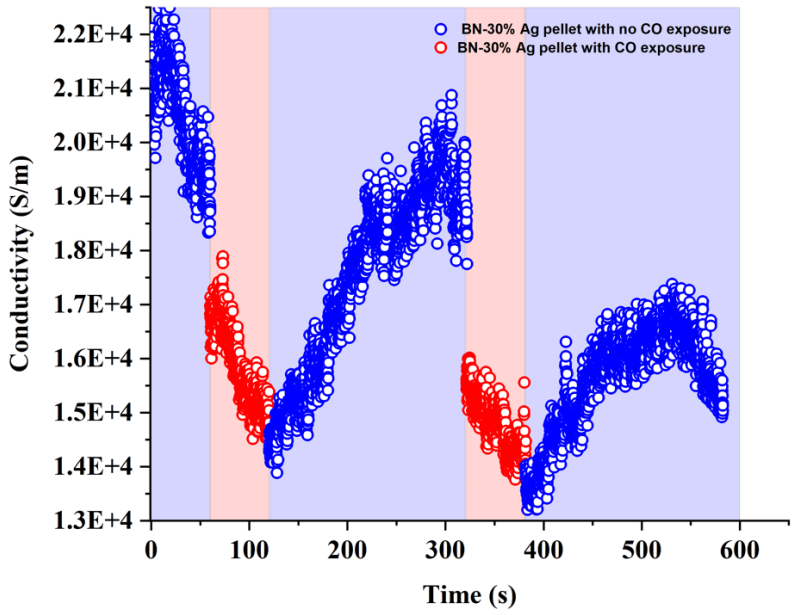

Figure 36: Conductivity results for h-BN-30wt.% Ag pellet under CO exposure.

As for the *h*-BN-30wt.% Ag pellet, figure 36, a high-baseline conductivity of 2.10×10^4 S/m, which immediately decreases by 24% to 1.60×10^4 S/m when exposed to CO. Following approximately 3 minutes of purging (no gas exposure), the specimen demonstrated a 90% recovery. A subsequent CO exposure induced an immediate 30% drop when the pellet was exposed to CO gas for a second time. Upon removing the target gas after this second cycle, the material stabilized at a new, shifted baseline conductivity of 1.6×10^4 S/m. Even though the testing is preliminary and future work might alter the composition of the material, the results presented indicate the potential of *h*-BN as a gas sensor.

CHAPTER VII

CONCLUSION

Infrastructure degradation results from local material failures and environmental factors. This problem is particularly prevalent in urban areas, where a growing population demands more accessible housing, utilities, and transportation. Developing quasi-real-time crack detection techniques that accurately assess the type, depth, and location of degradation is of great importance. The proposed research focuses on candidate materials for use in enhanced crack and gas detection technologies, which could significantly improve the safety, efficiency, and cost-effectiveness of infrastructure maintenance.

In Chapter 4, nanoparticles of (0.5, 3, 10 mol%) Er^{3+}-doped LT were synthesized using a technique that firstly transforms commercially available tantalum oxide particles into nanoscale particles. These particles were characterized by XRD to ensure the proper implementation of Er^{3+} to its host. XRD showed no peak shifts between the host LT and its doped counterparts. The DSC analysis showed a lower reaction initiation temperature for configuration 3 mol. % Er^{3+}-doped LT, which could be attributed to the creation of additional reaction hotspots in the system. The 3 mol. % Er^{3+}-doped LT configuration shows stronger visible photoluminescence emission compared to the system containing 0.5% and 10% Er^{3+}. However, the system with 0.5 mol.% Er^{3+} demonstrates improved near-IR emission than both 3% and 10% Er^{3+}-doped LT. Thus, the 0.5–3 mol% Er^{3+}-doped LT are strong candidates for an IR laser detector. The calculated

electronic and optical properties on LT and Er^{3+}-doped LT, using GGA, calculations showed that the location of the Er^{3+}- 4f bands depend on the metal site that Er occupies in lattice. The optical properties calculations show peaks that verify the presence of intraband transitions. The electronic structure is also calculated using the hybrid functional HSE06, which accurately locates the individual 4f orbitals in energy, thereby enabling interband transition assignments. All computational calculations presented agree with the experimental work performed.

In Chapter 5, DFT calculations were used to investigate the electronic and optical properties of Pr^{3+}-doped and Er^{3+}-/Pr^{3+}-co-doped LT. The PBE band structure and DOS results showed that the O 2p orbitals dominate the valence band, while Ta d states dominate the conduction band. The rare-earth 4f states strongly depend on the dopant type and substitutional site. For Pr^{3+}- substituting at the Li site, the Pr^{3+} 4f states appear near the conduction-band minimum, whereas Pr^{3+}- substitution at the Ta site produces split bands above the Fermi level and a dual-gap structure. In the Er^{3+}-/Pr^{3+}-co-doped configuration, hybridization between Er^{3+}-4f and Pr^{3+}-4f states broadens the f-manifold and enhances intraband f‑f optical transitions. HSE06 calculations provided a more reliable description of the band-gap magnitude and the energetic position of the 4f states. QTAIM and ELF analyses further clarified the nature of the metal‑oxygen interactions, revealing weak Li–O bonding and incipient covalent character in the Ta–O, Er–O, and Pr–O interactions. Experimentally, the photoluminescence spectra showed strong visible emissions near 600‑650 nm and infrared emissions in the 1050–1250 nm range, demonstrating that rare-earth doping and co-doping can tune the optical response of LT. These results highlight the structural and optical tunability of LT and support its potential use as a rare-earth-modified NIR sensing material.

In Chapter 6, Ag-decorated defect *h*-BN nanocomposites were synthesized and characterized to evaluate their potential for CO gas sensing. XRD and SEM analyses confirmed the formation of Ag/*h*-BN nanocomposites and showed that Ag nanoparticles were distributed on the h-BN surface. First-principles calculations, including DFT, G_0W_0, and BSE, were used to investigate pristine *h*-BN, vacancy-defective *h*-BN, Ag-decorated defective *h*-BN, and CO-adsorbed Ag-decorated *h*-BN configurations. Pristine *h*-BN showed strong B–N orbital hybridization, with N states dominating the valence-band edge and B states contributing primarily near the conduction-band edge. Vacancy defects significantly modified the electronic structure, and Ag decoration further altered the electronic and optical response. CO adsorption was found to be strongly defect-dependent: CO binds strongly at Ag-decorated B-vacancy sites, while the interaction at Ag-decorated N-vacancy sites is weak. The Ag-decorated B-vacancy configuration also produced stronger low-energy optical absorption, indicating enhanced optical sensitivity to CO. Experimentally, conductivity measurements showed that the *h*-BN–30 wt.% Ag pellet exhibited repeatable response, rapid detection, and recovery during purging, whereas the *h*-BN–80 wt.% Ag pellet showed stronger saturation and poor recovery. These results indicate that moderate Ag loading improves CO-sensing performance, while excessive Ag content hinders reversibility.

REFERENCES

1. Biezma, M.V. and F. Schanack, *Collapse of steel bridges.* Journal of Performance of Constructed Facilities, 2007. **21**(5): p. 398-405.
2. Choudhury, J.R. and A. Hasnat. *Bridge collapses around the world: Causes and mechanisms*. in *IABSE-JSCE joint conference on advances in bridge engineering-III, Dhaka, Bangladesh*. 2015.
3. Yao, Y., S.T.E. Tung, and B. Glisic, *Crack detection and characterization techniques—An overview.* Structural Control and Health Monitoring, 2014. **21**(12): p. 1387-1413.
4. Cross, E., K. Worden, and C. Farrar, *Structural health monitoring for civil infrastructure*, in *Health Assessment of Engineered Structures: Bridges, Buildings and Other Infrastructures*. 2013, World Scientific. p. 1-31.
5. Moomen, M., et al., *Bridge deterioration models to support Indiana's bridge management system.* 2016.
6. Darghiasi, P. and M. Shahandashti. *Examining Design, Construction, and Maintenance Procedures for Texas Off-System Bridges Managed by Local Governments*. in *International Conference on Transportation and Development 2024*. 2024.
7. O'Malley, C., et al., *CONDITION ASSESSMENT OF EXISTING BRIDGE STRUCTURES.* 2009.
8. Washer, G., et al., *Proposed guideline for reliability-based bridge inspection practices*. 2014.
9. Ryan, T.W., et al., *Bridge inspector's reference manual (BIRM).* 2022.
10. Shirato, M. and T. Tamakoshi. *Bridge inspection standards in Japan and US*. in *Proceedings os 29th US–Japan Bridge Engineering Workshop*. 2013.
11. Yeum, C.M., J. Choi, and S.J. Dyke, *Automated region-of-interest localization and classification for vision-based visual assessment of civil infrastructure.* Structural Health Monitoring, 2019. **18**(3): p. 675-689.
12. Rens, K.L., T.J. Wipf, and F.W. Klaiber, *Review of nondestructive evaluation techniques of civil infrastructure.* Journal of performance of constructed facilities, 1997. **11**(4): p. 152-160.
13. Chang, P.C., A. Flatau, and S.-C. Liu, *Health monitoring of civil infrastructure.* Structural health monitoring, 2003. **2**(3): p. 257-267.
14. Grosse, C.U., S.D. Glaser, and M. Kruger, *Initial development of wireless acoustic emission sensor Motes for civil infrastructure state monitoring.* Smart Structures and Systems, 2010. **6**(3): p. 197-209.
15. Heather-Smith, H., et al., *Monitoring buried infrastructure deformation using acoustic emissions.* 2018.

16. Alqurashi, I., et al., *A review of ultrasonic testing and evaluation methods with applications in civil NDT/E.* Journal of Nondestructive Evaluation, 2025. **44**(2): p. 53.
17. Afrasiabi, A., F. Rahimzadeh, and A. Keshavarzi, *Advances in electromagnetic techniques for subsurface infrastructure detection: A comprehensive review of methods, challenges, and innovations.* arXiv preprint arXiv:2511.22673, 2025.
18. Garrido, I., et al., *Thermographic methodologies used in infrastructure inspection: A review—data acquisition procedures.* Infrared Physics & Technology, 2020. **111**: p. 103481.
19. Singh, Y., et al., *Highly responsive near-infrared Si/Sb2Se3 photodetector via surface engineering of silicon.* ACS Applied Materials & Interfaces, 2023. **15**(25): p. 30443-30454.
20. Yamazoe, N. and N. Miura, *Development of gas sensors for environmental protection.* IEEE Transactions on Components, Packaging, and Manufacturing Technology: Part A, 2002. **18**(2): p. 252-256.
21. Kjaer, K.H. and C.-O. Ottosen, *3D laser triangulation for plant phenotyping in challenging environments.* Sensors, 2015. **15**(6): p. 13533-13547.
22. Ernst, A. and J.D. Zibrak, *Carbon monoxide poisoning.* New England journal of medicine, 1998. **339**(22): p. 1603-1608.
23. Savioli, G., et al., *Carbon monoxide poisoning: from occupational health to emergency medicine.* Journal of clinical medicine, 2024. **13**(9): p. 2466.
24. Kohl, D., *Function and applications of gas sensors.* Journal of Physics D: Applied Physics, 2001. **34**(19): p. R125-R149.
25. Krishna Prasad, N., et al., *Ceramic Sensors: A mini-review of their applications.* Frontiers in Materials, 2020. **7**: p. 593342.
26. Ikhmayies, S.J., *Advanced ceramics*. 2024: Springer.
27. Dineva, P., et al., *Piezoelectric materials*, in *Dynamic Fracture of Piezoelectric Materials: Solution of Time-Harmonic Problems via BIEM*. 2014, Springer. p. 7-32.
28. Silvestri, L., *Nano-Optics for Enhancing Light-Matter Interactions on a Molecular Scale: Plasmonics, Photonic Materials and Sub-Wavelength Resolution*. 2012: Springer.
29. Matthias, B. and J. Remeika, *Ferroelectricity in the ilmenite structure.* Physical Review, 1949. **76**(12): p. 1886.
30. Whatmore, R., *Ferroelectric materials*, in *Springer handbook of electronic and photonic materials*. 2017, Springer. p. 1-1.
31. Schweinler, H.C., *Ferroelectricity in the ilmenite structure.* Physical Review, 1952. **87**(1): p. 5.
32. Uchino, K., *Ferroelectric devices*. 2018: CRC press.
33. Si, J., et al., *Pyroelectric properties and applications of lithium tantalate crystals.* Crystals, 2024. **14**(7): p. 579.
34. Bravina, S.L., et al., *Investigations of LiNbO3 and LiTaO3 single crystals for pyroelectric applications in the wide temperature range.* Ferroelectrics, 2007. **353**(1): p. 202-211.
35. Glass, A. and M. Lines, *Low-temperature behavior of spontaneous polarization in LiNb O 3 and LiTa O 3.* Physical Review B, 1976. **13**(1): p. 180.
36. Furukawa, Y., et al., *Stoichiometric LiTaO3 single crystal growth by double crucible Czochralski method using automatic powder supply system.* Journal of crystal growth, 1999. **197**(4): p. 889-895.

37. Kumaragurubaran, S., et al., *Growth of 4-in diameter near-stoichiometric lithium tantalate single crystals.* Journal of crystal growth, 2005. **285**(1-2): p. 88-95.
38. Patil, K.C., S.T. Aruna, and S. Ekambaram, *Combustion synthesis.* Current opinion in solid state and materials science, 1997. **2**(2): p. 158-165.
39. Zhu, Y., et al., *Efficient synthesis of stoichiometric lithium tantalate powder by a solid-state combustion route.* Materials and manufacturing processes, 2015. **30**(11): p. 1342-1347.
40. Muthurajan, H., et al., *A novel technique to prepare LiTaO3 at low temperature.* Ceramics international, 2008. **34**(3): p. 669-670.
41. Bonnelle, C. and N. Spector, *Rare-earths and actinides in high energy spectroscopy*. 2015: Springer.
42. Yang, X., et al., *Luminescent properties of stoichiometric Er: LiTaO3 submicron particles synthesized by a modified solid-state combustion route.* Ceramics International, 2019. **45**(8): p. 10733-10739.
43. Shi, L., et al., *White upconversion emission in Er3+/Yb3+/Tm3+ codoped LiTaO3 polycrystals.* Journal of alloys and compounds, 2014. **591**: p. 105-109.
44. Li, X., et al., *Intense mechanoluminescence and photostimulated luminescence with less afterglow in Pr3+/Gd3+ co-doped LiTaO3 phosphors.* Journal of Luminescence, 2021. **238**: p. 118222.
45. Liu, X., et al., *A survey on gas sensing technology.* Sensors, 2012. **12**(7): p. 9635-9665.
46. Bogue, R., *Detecting gases with light: a review of optical gas sensor technologies.* Sensor Review, 2015. **35**(2): p. 133-140.
47. Hodgkinson, J. and R.P. Tatam, *Optical gas sensing: a review.* Measurement science and technology, 2013. **24**(1): p. 012004.
48. Grate, J.W., S.J. Martin, and R.M. White, *Acoustic wave microsensors.* analytical Chemistry, 1993. **65**(21): p. 940A-948A.
49. Li, X., et al., *Advances in sensing mechanisms and micro/nanostructured sensing layers for surface acoustic wave-based gas sensors.* Journal of Materials Chemistry A, 2023. **11**(17): p. 9216-9238.
50. Dressler, M., *Selective gas chromatographic detectors*. Vol. 36. 1986: Elsevier.
51. Khan, M.A.H., M.V. Rao, and Q. Li, *Recent advances in electrochemical sensors for detecting toxic gases: NO2, SO2 and H2S.* Sensors, 2019. **19**(4): p. 905.
52. Miyake, M., *Electrochemical functions*, in *Carbon alloys*. 2003, Elsevier. p. 435-445.
53. Pavel, I.-A., S. Lakard, and B. Lakard, *Flexible sensors based on conductive polymers.* Chemosensors, 2022. **10**(3): p. 97.
54. Byeon, J.-H., et al., *Acetone gas sensor based on SWCNT/polypyrrole/phenyllactic acid nanocomposite with high sensitivity and humidity stability.* Biosensors, 2022. **12**(5): p. 354.
55. Li, Y., et al., *A novel gas sensor for detecting pork freshness based on PANI/AgNWs/silk.* Foods, 2022. **11**(15): p. 2372.
56. Dong, R., et al., *Conducting polymers-based gas sensors: Principles, materials, and applications.* Sensors, 2025. **25**(9): p. 2724.
57. Dipak, P., et al., *Synthesis of polyaniline (printable nanoink) gas sensor for the detection of ammonia gas.* Journal of Materials Science: Materials in Electronics, 2020. **31**(24): p. 22512-22521.

58. Elhaes, H., A. Fakhry, and M. Ibrahim, *Carbon nano materials as gas sensors.* Materials Today: Proceedings, 2016. **3**(6): p. 2483-2492.
59. Llobet, E., *Gas sensors using carbon nanomaterials: A review.* Sensors and Actuators B: Chemical, 2013. **179**: p. 32-45.
60. Dey, A., *Semiconductor metal oxide gas sensors: A review.* Materials science and Engineering: B, 2018. **229**: p. 206-217.
61. Kadiyala, K.G. and N.K. Katari, *Ceramics for sensing application*, in *Advanced Ceramic Coatings for Emerging Applications*. 2023, Elsevier. p. 71-84.
62. Nenov, T. and S.P. Yordanov, *Ceramic sensors: technology and applications*. 2020: CRC press.
63. Ribeiro, M.J. and D. Tulyaganov, *Traditional ceramics manufacturing*, in *Ceramics, Glass and Glass-Ceramics: From Early Manufacturing Steps towards Modern Frontiers*. 2021, Springer. p. 75-118.
64. Heimann, R.B., *Classic and advanced ceramics: from fundamentals to applications*. 2010: John Wiley & Sons.
65. Ikhmayies, S.J., *Advanced Ceramics*. 1 ed. Advances in Material Research and Technology. 2023, Cham: Springer.
66. Nenov, T. and S. Yordanov, *Ceramic sensor device materials.* Sensors and Actuators B: Chemical, 1992. **8**(1): p. 117-122.
67. Ramanavicius, S., et al., *TiO2-x/TiO2-structure based 'self-heated'sensor for the determination of some reducing gases.* Sensors, 2019. **20**(1): p. 74.
68. Lü, R., et al., *Alumina decorated TiO 2 nanotubes with ordered mesoporous walls as high sensitivity NO x gas sensors at room temperature.* Nanoscale, 2013. **5**(18): p. 8569-8576.
69. Galstyan, V., et al., *TiO2 nanotubes: recent advances in synthesis and gas sensing properties.* Sensors, 2013. **13**(11): p. 14813-14838.
70. Ramanavicius, S., A. Jagminas, and A. Ramanavicius, *Gas sensors based on titanium oxides.* Coatings, 2022. **12**(5): p. 699.
71. Kumar, R., et al., *Zinc oxide nanostructures for NO2 gas–sensor applications: A review.* Nano-Micro Letters, 2015. **7**(2): p. 97-120.
72. Jamshidi Bandari, A. and S. Nasirian, *Carbon monoxide gas sensing features of zinc oxide nanoneedles: practical selectivity and long-term stability.* Journal of Materials Science: Materials in Electronics, 2019. **30**(11): p. 10073-10081.
73. Kolekar, T., et al., *Synthesis and characterization of ZnO nanoparticles for efficient gas sensors.* Arch. Appl. Sci. Res, 2013. **5**(6): p. 20-28.
74. Calestani, D., et al., *Growth of ZnO tetrapods for nanostructure-based gas sensors.* Sensors and Actuators B: Chemical, 2010. **144**(2): p. 472-478.
75. Zhang, J., et al., *ZnO hollow spheres: preparation, characterization, and gas sensing properties.* Sensors and Actuators B: Chemical, 2009. **139**(2): p. 411-417.
76. Shen, Z.-Y., et al., *Study on performance improvement of zinc oxide gas sensor with silver nanoparticles surface modification.* Sensors and Actuators B: Chemical, 2025. **438**: p. 137803.
77. Cheng, J., et al., *A review of recent developments in tin dioxide composites for gas sensing application.* Journal of Industrial and Engineering Chemistry, 2016. **44**: p. 1-22.
78. Pandit, N.A. and T. Ahmad, *Tin oxide based hybrid nanostructures for efficient gas sensing.* Molecules, 2022. **27**(20): p. 7038.

79. Berger, F., J.-B. Sanchez, and O. Heintz, *Detection of hydrogen fluoride using SnO2-based gas sensors: Understanding of the reactional mechanism.* Sensors and Actuators B: Chemical, 2009. **143**(1): p. 152-157.
80. Zhang, Y., et al., *Adsorption of NO2, NO, NH3, and CO on Noble Metal (Rh, Pd, Ag, Ir, Pt, Au)-Modified Hexagonal Boron Nitride Monolayers: A First-Principles Study.* Langmuir, December 26, 2023. **40**(1).
81. Garnica, M., et al., *Comparative study of the interfaces of graphene and hexagonal boron nitride with silver.* Physical Review B, 2016-10-18. **94**(15).
82. *Development of gas sensors for environmental protection.* IEEE Transactions on Components, Packaging, and Manufacturing Technology: Part A, 1995. **18**(2).
83. Yan Zhang, et al., *Synthesis and modification of boron nitride nanomaterials for gas sensors: from theory to application.* Physical Chemistry Chemical Physics, 2024/11/20. **26**(45).
84. Ahmed, M.T., et al., *First principles investigations of Cobalt and Manganese doped boron nitride nanosheet for gas sensing application.* Applied Surface Science, 2023/06/30. **623**.
85. Goel, N., et al., *Recent advances in ultrathin 2D hexagonal boron nitride based gas sensors.* Journal of Materials Chemistry C, 2021/02/15. **9**(5).
86. Yu, Y. and C. Dai, *DFT study of gas adsorption and sensing based on noble metal (Ag, Au and Pt) functionalized boron selenide nanosheets.* Physica E: Low-dimensional Systems and Nanostructures, 2021/01/01. **125**.
87. Giovannetti, G., et al., *Substrate-induced band gap in graphene on hexagonal boron nitride: Ab initio density functional calculations.* Physical Review B, 2007-08-16. **76**(7).
88. Lin, S., et al., *First-principles investigations of metal (Cu, Ag, Au, Pt, Rh, Pd, Fe, Co, and Ir) doped hexagonal boron nitride nanosheets: stability and catalysis of CO oxidation.* The Journal of Physical Chemistry C, 2013. **117**(33): p. 17319-17326.
89. Sajjad, M. and P. Feng, *Study the gas sensing properties of boron nitride nanosheets.* Materials Research Bulletin, 2014. **49**: p. 35-38.
90. Lin, L., et al., *Synthesis of boron nitride nanosheets with a few atomic layers and their gas-sensing performance.* Ceramics International, 2016. **42**(1): p. 971-975.
91. *From Being to Becoming: Time and Complexity in the Physical Sciences.* Reviews, 1982-01-01T05:00:00. **35**(1).
92. Schrödinger, E., *An Undulatory Theory of the Mechanics of Atoms and Molecules.* Physical Review, 1926-12-01. **28**(6).
93. Aharonov, Y., J. Anandan, and L. Vaidman, *Meaning of the wave function.* Physical Review A, 1993-06-01. **47**(6).
94. Sholl, D.S., J.A. Steckel, and Sholl, *Density Functional Theory : A Practical Introduction*. 2009, Hoboken, UNITED STATES: John Wiley & Sons, Incorporated.
95. Somsikov, V. and V. Somsikov, *Extension of the Schrodinger equation.* European Physical Journal Web of Conferences, 03/2017. **138**.
96. Dorling, J., *Schrödinger's original interpretation of the Schrödinger equation.* Schrödinger: Centenary celebration of a polymath, 1987: p. 16.
97. Lykos, P. and G.W. Pratt, *Discussion on The Hartree-Fock Approximation.* Reviews of Modern Physics, 1963-07-01. **35**(3).
98. Sherrill, C.D., *An introduction to Hartree-Fock molecular orbital theory.* School of Chemistry and Biochemistry Georgia Institute of Technology, 2000. **1**.

99. Pauling, L. and E.B. Wilson, *Introduction to quantum mechanics with applications to chemistry*. 2012: Courier Corporation.
100. Hartree, D.R. and W. Hartree, *Self-consistent field, with exchange, for beryllium.* Proceedings of the Royal Society of London. A. Mathematical and Physical Sciences, 1935/05/01. **150**(869).
101. Szabo, A. and N.S. Ostlund, *Modern quantum chemistry: introduction to advanced electronic structure theory*. 2012: Courier Corporation.
102. Messiah, A., *Quantum mechanics*. 2014: Courier Corporation.
103. Hohenberg, P. and W. Kohn, *Inhomogeneous Electron Gas.* Physical Review, 1964-11-09. **136**(3B).
104. Qian, Z. and V. Sahni, *Physics of transformation from Schr\"odinger theory to Kohn-Sham density-functional theory: Application to an exactly solvable model.* Physical Review A, 1998-04-01. **57**(4).
105. Anisimov, V.I. and O. Gunnarsson, *Density-functional calculation of effective Coulomb interactions in metals.* Physical Review B, 1991-04-01. **43**(10).
106. Kohn, W. and L.J. Sham, *Self-Consistent Equations Including Exchange and Correlation Effects.* Physical Review, 1965-11-15. **140**(4A).
107. Garza, J., J.A. Nichols, and D.A. Dixon, *The Hartree product and the description of local and global quantities in atomic systems: A study within Kohn–Sham theory.* The Journal of Chemical Physics, 2000/01/15. **112**(3).
108. Handler, G.S., *Exchange energy in the Thomas-Fermi model.* The Journal of Chemical Physics, 1974/12/01. **61**(11).
109. Lewin, M., E.H. Lieb, and R. Seiringer, *The Local Density Approximation in Density Functional Theory.* 2019/03/10.
110. *Density Functional Theory.* 1990.
111. Burke, K. and L.O. Wagner, *DFT in a nutshell.* International Journal of Quantum Chemistry, 2013/01/15. **113**(2).
112. Simón, L., et al., *How reliable are DFT transition structures? Comparison of GGA, hybrid-meta-GGA and meta-GGA functionals.* Organic & Biomolecular Chemistry, 2011/01/19. **9**(3).
113. Hua, X., X. Chen, and W. Goddard, *Generalized generalized gradient approximation: An improved density-functional theory for accurate orbital eigenvalues.* Physical Review B, 1997. **55**(24): p. 16103.
114. Perdew, J.P., K. Burke, and M. Ernzerhof, *Generalized Gradient Approximation Made Simple.* Physical Review Letters, 1996-10-28. **77**(18).
115. Becke, A.D., *A new mixing of Hartree–Fock and local density-functional theories.* The Journal of Chemical Physics, 1993/01/15. **98**(2).
116. Koller, D., P. Blaha, and F. Tran, *Hybrid functionals for solids with an optimized Hartree-Fock mixing parameter.* 2013/04/16.
117. Heyd, J., G.E. Scuseria, and M. Ernzerhof, *Hybrid functionals based on a screened Coulomb potential.* The Journal of Chemical Physics, 2003/05/08. **118**(18).
118. Skelton, J.M., et al., *Accuracy of Hybrid Functionals with Non-Self-Consistent Kohn–Sham Orbitals for Predicting the Properties of Semiconductors.* Journal of Chemical Theory and Computation, May 5, 2020. **16**(6).
119. Haas, P., et al., *Insight into the performance of GGA functionals for solid-state calculations.* Physical Review B, 2009-11-12. **80**(19).

120. Wannier, G.H., *The Structure of Electronic Excitation Levels in Insulating Crystals.* Physical Review, 1937-08-01. **52**(3).
121. Bloch, I., J. Dalibard, and W. Zwerger, *Many-body physics with ultracold gases.* Reviews of Modern Physics, 2008-07-18. **80**(3).
122. Kohn, W., *Construction of Wannier Functions and Applications to Energy Bands.* Physical Review B, 1973-05-15. **7**(10).
123. Martin, P.C. and J. Schwinger, *Theory of Many-Particle Systems. I.* Physical Review, 1959-09-15. **115**(6).
124. Rizzo, J., et al., *One-particle Green's functions from the quantum equation of motion algorithm.* Physical Review Research, 2022-10-07. **4**(4).
125. Aryasetiawan, F., et al., *The GW method.* Reports on Progress in Physics, 1998-03-01. **61**(3).
126. Marder, M.P., *Condensed matter physics*. 2010: John Wiley & Sons.
127. Riva, G., P. Romaniello, and J.A. Berger, *Multichannel Dyson Equation: Coupling Many-Body Green's Functions.* Physical Review Letters, 2023-11-20. **131**(21).
128. Held, K., et al., *Hedin equations, GW, GW+ DMFT, and all that.* arXiv preprint arXiv:1109.3972, 2011.
129. Hedin, L., *New Method for Calculating the One-Particle Green's Function with Application to the Electron-Gas Problem.* Physical Review, 1965-08-02. **139**(3A).
130. Reining, L., *The GW approximation: content, successes and limitations.* Wiley Interdisciplinary Reviews: Computational Molecular Science, 2018. **8**(3): p. e1344.
131. *GW method and Bethe–Salpeter equation for calculating electronic excitations.* WIREs Computational Molecular Science, 2016. **6**(5).
132. Strinati, G. and G. Strinati, *Application of the Green's functions method to the study of the optical properties of semiconductors.* La Rivista del Nuovo Cimento (1978-1999) 1988 11:12, 2008-09-17. **11**(12).
133. Riess, J. and W. Münch, *The theorem of Hohenberg and Kohn for subdomains of a quantum system.* Theoretica chimica acta, 1981. **58**(4): p. 295-300.
134. Bader, R.F., *Atoms in molecules.* Accounts of chemical research, 1985. **18**(1): p. 9-15.
135. Bader, R. and P. Becker, *Transferability of atomic properties and the theorem of Hohenberg and Kohn.* Chemical physics letters, 1988. **148**(5): p. 452-458.
136. Vega, D. and D. Almeida, *AIM-UC: An application for QTAIM analysis.* Journal of Computational Methods in Science and Engineering, 2014. **14**(1-3): p. 131-136.
137. Cortés-Guzmán, F., J.I. Rodríguez, and J.S. Anderson, *Introduction to QTAIM and beyond*, in *Advances in quantum chemical topology beyond QTAIM*. 2023, Elsevier. p. 1-19.
138. Espinosa, E., et al., *From weak to strong interactions: A comprehensive analysis of the topological and energetic properties of the electron density distribution involving X–H⋯F–Y systems.* The Journal of chemical physics, 2002. **117**(12): p. 5529-5542.
139. Fuentealba, P., E. Chamorro, and J.C. Santos, *Understanding and using the electron localization function*, in *Theoretical and computational chemistry*. 2007, Elsevier. p. 57-85.
140. Becke, A.D. and K.E. Edgecombe, *A simple measure of electron localization in atomic and molecular systems.* 1990. **92**: p. 5397-5403.

141. Payne, M.C., et al., *Iterative minimization techniques for ab initio total-energy calculations: molecular dynamics and conjugate gradients.* Reviews of Modern Physics, 1992-10-01. **64**(4).
142. Clark, S.J., et al., *First principles methods using CASTEP.* Zeitschrift für Kristallographie - Crystalline Materials, 2005. **220**(5-6).
143. Niibe, M., et al., *Application of CASTEP Code to the Simulation of Soft X-ray Emission Spectra of Light Element Materials.* e-Journal of Surface Science and Nanotechnology, 2025.
144. Segall, M.D., et al., *First-principles simulation: ideas, illustrations and the CASTEPcode.* Journal of Physics: Condensed Matter, 2002-03-08. **14**(11).
145. Giannozzi, P., et al., *Advanced capabilities for materials modelling with Quantum ESPRESSO.* Journal of Physics: Condensed Matter, 2017-10-24. **29**(46).
146. Giannozzi, P., et al., *QUANTUM ESPRESSO: a modular and open-source software project for quantumsimulations of materials.* Journal of Physics: Condensed Matter, 2009-09-01. **21**(39).
147. Hafner, J., *Ab-initio simulations of materials using VASP: Density-functional theory and beyond.* Journal of Computational Chemistry, 2008/10/01. **29**(13).
148. Schloegl, R., *X-ray Diffraction: A Basic Tool for Characterization of Solid Catalysts in the Working State.* Advances in Catalysis, 2009. **52**: p. 273-338.
149. Jauncey, G.E.M. and G.E.M. Jauncey, *The Scattering of X-Rays and Bragg's Law.* Proceedings of the National Academy of Sciences, 1924-02. **10**(2).
150. Hargreaves, J.S.J., *Some considerations related to the use of the Scherrer equation in powder X-ray diffraction as applied to heterogeneous catalysts.* Catalysis, Structure & Reactivity, 2016-10-1. **2**(1-4).
151. Suryanarayana, C., *Mechanical alloying and milling.* Progress in Materials Science, 2001/01/01. **46**(1-2).
152. Baláž, P., *High-Energy Milling.* 2008.
153. Koch, C.C. and J.D. Whittenberger, *Mechanical milling/alloying of intermetallics.* Intermetallics, 1996/01/01. **4**(5).
154. McGonigle, R., et al., *Autoclave reactor synthesis of upconversion nanoparticles, unreported variables, and safety considerations.* Communications Chemistry 2025 8:1, 2025-02-06. **8**(1).
155. Alli, U., S.J. Hettiarachchi, and S. Kellici, *Chemical Functionalisation of 2D Materials by Batch and Continuous Hydrothermal Flow Synthesis.* Chemistry – A European Journal, 2020/05/20. **26**(29).
156. Suárez, M., et al., *Challenges and Opportunities for Spark Plasma Sintering: A Key Technology for.* Sintering applications, 2013. **319**.
157. Hobosyan, M.A., et al., *Computational and experimental study on undoped and Er-doped lithium tantalate nanofluorescent probes.* Materials Today Communications, 2023. **36**: p. 106503.
158. Muthurajan, H., et al., *A novel technique to prepare LiTaO3 at low temperature.* Ceramics International, 2008/04/01. **34**(3).
159. Callister Jr, W.D. and D.G. Rethwisch, *Materials science and engineering: an introduction*. 2020: John wiley & sons.
160. Toriyama, M.Y., et al., *How to analyse a density of states.* Materials today electronics, 2022. **1**: p. 100002.

161. Ibach, H. and H. Lüth, *Solid-state physics: an introduction to principles of materials science*. 2013: Springer Science & Business Media.
162. Zangwill, A., *Modern electrodynamics*. 2013: Cambridge University Press.
163. Dressel, M. and G. Grüner, *Electrodynamics of solids: optical properties of electrons in matter*. 2002: Cambridge university press.
164. Politano, G.G. and C. Versace, *Spectroscopic ellipsometry: advancements, applications and future prospects in optical characterization.* Spectroscopy Journal, 2023. **1**(3): p. 163-181.
165. Hilfiker, J.N. and T. Tiwald, *Dielectric function modeling*, in *Spectroscopic Ellipsometry for Photovoltaics: Volume 1: Fundamental Principles and Solar Cell Characterization*. 2019, Springer. p. 115-153.
166. Grosse, P. and V. Offermann, *Analysis of reflectance data using the Kramers-Kronig relations.* Applied Physics A, 1991. **52**(2): p. 138-144.
167. Zych, E. and E. Zych, *Concentration dependence of energy transferbetween Eu3+ ions occupying two symmetry sites inLu2O3.* Journal of Physics: Condensed Matter, 2002-05-23. **14**(22).
168. Dai, S., et al., *Concentration quenching in erbium-doped tellurite glasses.* Journal of Luminescence, 2006/03/01. **117**(1).
169. Benz, F. and H.P. Strunk, *Rare earth luminescence: A way to overcome concentration quenching.* AIP Advances, 2012/12/01. **2**(4).
170. Kutzelnigg, W., et al., *Hund's rules.* Zeitschrift für Physik D Atoms, Molecules and Clusters 1996 36:3, 1996/09. **36**(3).
171. Dimakis, N., et al., *Erbium and praseodymium doped lithium tantalate electronic structure and metal-oxygen bonding analyses.* Materials Today Communications, 2025. **44**: p. 112047.
172. Sultan, A. and F. Mohammad, *Chemical sensing, thermal stability, electrochemistry and electrical conductivity of silver nanoparticles decorated and polypyrrole enwrapped boron nitride nanocomposite.* Polymer, 2017/03/24. **113**.
173. Lin, Z., et al., *Defect engineering of two-dimensional transition metal dichalcogenides.* 2D Materials, 2016. **3**(2): p. 022002.
174. Innocenzi, P. and L. Stagi, *From defects to photoluminescence in h-BN 2D and 0D nanostructures.* Accounts of Materials Research, 2024. **5**(4): p. 413-425.
175. Solozhenko, V.L., et al., *Bandgap energy of graphite-like hexagonal boron nitride.* Journal of Physics and Chemistry of Solids, 2001. **62**(7): p. 1331-1334.
176. Callister Jr, W.D., *Materials Science and Engineering - An Introduction (5th ed.).* Anti-Corrosion Methods and Materials, 2000. **47**(1).

VITA

Andrea Pelayo Carvajal attended the Mathematics and Science Academy at the University of Texas Rio Grande Valley and graduated in May 2020. The following August she entered the University of Texas Rio Grande Valley, and in December 2023 received the degree of Bachelor of Science in Physics with a minor in Mechanical Engineering. Andrea continued her graduate studies at the University of Texas Rio Grande Valley and received the degree of Doctor of Philosophy in Physics in July 2026. Andrea Pelayo can be reached at andrea.pelayocarvajal@gmail.com